

THE *SPITZER* c2d SURVEY OF LARGE, NEARBY, INTERSTELLAR CLOUDS. I. CHAMAELEON II OBSERVED WITH MIPS

KAISA E. YOUNG,¹ PAUL M. HARVEY,¹ TIMOTHY Y. BROOKE,² NICHOLAS CHAPMAN,³ JENS KAUFFMANN,⁴ FRANK BERTOLDI,⁵
SHIH-PING LAI,³ JUAN ALCALÁ,⁶ TYLER L. BOURKE,⁷ WILLIAM SPIESMAN,¹ LORI E. ALLEN,⁷ GEOFFREY A. BLAKE,⁸
NEAL J. EVANS II,¹ DAVID W. KOERNER,⁹ LEE G. MUNDY,³ PHILIP C. MYERS,⁷ DEBORAH L. PADGETT,¹⁰
ANANDI SALINAS,¹ ANNEILA I. SARGENT,² KARL R. STAPELFELDT,¹¹ PETER TEUBEN,³
EWINE F. VAN DISHOCK,¹² AND ZAHED WAHHAJ⁹
Received 2005 February 15; accepted 2005 March 29

ABSTRACT

We present maps of over 1.5 deg² in Chamaeleon (Cha) II at 24, 70, and 160 μm observed with the *Spitzer Space Telescope* Multiband Imaging Photometer for *Spitzer* (MIPS) and a 1.2 deg² millimeter map from SIMBA on the Swedish-ESO Submillimetre Telescope (SEST). The c2d *Spitzer* Legacy Team’s data reduction pipeline is described in detail. Over 1500 24 μm sources and 41 70 μm sources were detected by MIPS with fluxes greater than 10 σ . More than 40 potential YSOs are identified with a MIPS and 2MASS color-color diagram and by their spectral indices, including two previously unknown sources with 24 μm excesses. Our new SIMBA millimeter map of Cha II shows that only a small fraction of the gas is in compact structures with high column densities. The extended emission seen by MIPS is compared with previous CO observations. Some selected interesting sources, including two detected at 1 mm, associated with Cha II are discussed in detail, and their SEDs are presented. The classification of these sources using MIPS data is found to be consistent with that of previous studies.

Subject headings: infrared: stars — ISM: clouds — stars: formation

1. INTRODUCTION

The Chamaeleon (Cha) II molecular cloud is one of five clouds that were mapped with the *Spitzer Space Telescope* as part of the “From Molecular Cores to Planet-forming Disks” Legacy project (Evans et al. 2003). The main goal of the “cores to disks” (c2d) Legacy project is to study the evolution of star and planet formation from cold molecular cores to protoplanetary disks in a range of environments. The project makes use of all the instruments on *Spitzer* (the Multiband Imaging Photometer for *Spitzer* [MIPS], the Infrared Array Camera [IRAC], and the InfraRed

Spectrograph [IRS]) to observe nearby molecular clouds, isolated regions of star formation, and young stellar objects (YSOs), defined broadly in this work as sources with infrared excesses. One goal of the c2d project is to survey the YSO population of the five large molecular clouds for new candidate protostars, as well as substellar objects down to 0.001 L_{\odot} . This work describes MIPS observations of one of the molecular clouds mapped by c2d, Cha II, and is the first of a series of papers that present initial results from the c2d observations. We also present a new millimeter map of Cha II from SIMBA (SEST Imaging Bolometer Array) on the Swedish-ESO Submillimetre Telescope (SEST). The IRAC observations of Cha II will be described by A. Porras et al. (2005, in preparation). Later papers will follow that combine the data from all the *Spitzer* observations, as well as complementary observations at other wavelengths, and include further analysis of the YSOs and cloud environments.

Chamaeleon is a star-forming region in the southern sky that includes at least half a dozen distinct clouds (Boulanger et al. 1998). Cha II ($\alpha = 13^{\text{h}}$, $\delta = -77^{\circ}$ [J2000.0]), at a distance of 178 ± 18 pc (Whittet et al. 1997), is known to harbor dense molecular cores (Mizuno et al. 1999), T Tauri stars, and YSOs (Schwartz 1977; Whittet et al. 1991; Hughes & Hartigan 1992; Prusti et al. 1992; Vuong et al. 2001). Pointed *ROSAT* (*Röntgen-Satellit*) observations revealed many X-ray sources in Cha II, including weak-line and classical T Tauri stars (Alcalá et al. 2000). In addition to low-mass young stars, one intermediate-mass Ae star, DK Cha (IRAS 12496–7650), and the well-studied Herbig-Haro object HH 54 (e.g., Knee 1992; Liseau et al. 1996; Neufeld et al. 1998) are also associated with Cha II. Persi et al. (2003) studied a portion of Cha II ($28' \times 26'$) near the Class I source IRAS 12553–7651 (ISO-Cha II-28) in the mid-infrared (6.75 and 14.3 μm) with ISOCAM on the *Infrared Space Observatory* (ISO) satellite, as well as with near-infrared images, and found four new candidate YSOs (see their Table 4) in the observed region. Our MIPS survey of Cha II covers more area

¹ Department of Astronomy, University of Texas at Austin, 1 University Station C1400, Austin, TX 78712-0259; kaisa@astro.as.utexas.edu, pmh@astro.as.utexas.edu, spies@astro.as.utexas.edu, nje@astro.as.utexas.edu.

² Division of Physics, Mathematics, and Astronomy, MS 105-24, California Institute of Technology, Pasadena, CA 91125; tyb@astro.caltech.edu, afs@astro.caltech.edu.

³ Department of Astronomy, University of Maryland, College Park, MD 20742; chapman@astro.umd.edu, slai@astro.umd.edu, lgm@astro.umd.edu.

⁴ Max-Planck-Institut für Radioastronomie, Auf den Hügel 69, D-53121 Bonn, Germany; jkauffma@mpifr-bonn.mpg.de.

⁵ Radioastronomisches Institut der Universität Bonn, Auf den Hügel 71, D-53121 Bonn, Germany; bertoldi@uni-bonn.de.

⁶ INAF-Osservatorio Astronomico di Capodimonte, via Moiariello 16, 80131 Naples, Italy; jmae@sun1.na.astro.it.

⁷ Smithsonian Astrophysical Observatory, 60 Garden Street, Mail Stop 42, Cambridge, MA 02138; leallen@cfa.harvard.edu, tbourke@cfa.harvard.edu, pmyers@cfa.harvard.edu.

⁸ Division of Geological and Planetary Sciences, Mail Stop 150-21, California Institute of Technology, Pasadena, CA 91125; gab@gps.caltech.edu.

⁹ Department of Physics and Astronomy, Northern Arizona University, Box 6010, Flagstaff, AZ 86011-6010; koerner@physics.nau.edu, zwahhaj@physics.nau.edu.

¹⁰ *Spitzer* Science Center, MC 220-6, Pasadena, CA 91125; dlp@ipac.caltech.edu.

¹¹ Jet Propulsion Laboratory, Mail Stop 183-900, California Institute of Technology, 4800 Oak Grove Drive, Pasadena, CA 91109; krs@exoplanet.jpl.nasa.gov.

¹² Leiden Observatory, Postbus 9513, 2300 RA Leiden, Netherlands.

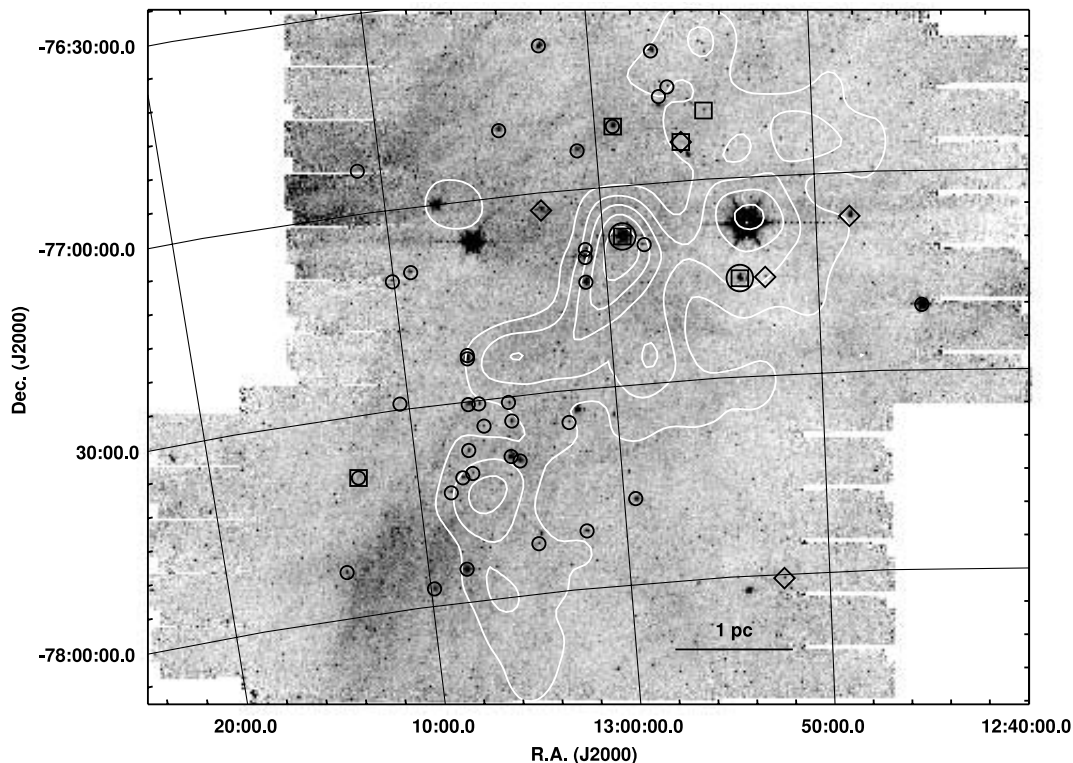


FIG. 1.—MIPS 24 μm map of the Cha II molecular cloud with A_V contours from Vuong et al. (2001; white). The contours are $A_V = 2\text{--}10$ mag by 2 mag. The circles and diamonds indicate the positions of the sources listed in Table 2. The different symbols identify the class of the object according to the $\alpha_{24/K}$ given in the table. Class I sources are represented by large circles, Class II by small circles, and Class III by diamonds. The squares mark the positions of the selected sources discussed in § 5. The three brightest sources from east to west are IRAS 13022–7650 (DL Cha, a variable star), IRAS 12553 (Class I), and IRAS 12496 (DK Cha, an Ae star). Latent images are seen as a line of dots to the east and west of these sources. The bright source to the northeast of IRAS 13022 at -77° is IRAS 13036 (Class 0 or I) in the molecular core BHR 86.

(about 7 times) at longer wavelengths (24, 70, and 160 μm) than the *ISO* observations and with greater sensitivity ($1\sigma \approx 0.15$ mJy at 24 μm vs. 1.3 mJy at 14 μm).

The five clouds in the c2d survey were chosen to span a range of star formation conditions. Cha II is one of the most quiescent of the clouds, with only a few known very young (Class I) objects. Most of the more than 30 previously identified YSOs in Cha II are T Tauri stars. Cha II is a typical site of low-mass star formation compared with other regions, with a star formation efficiency ($\sim 1\%$; Mizuno et al. 1999) similar to that of Taurus (2%; Mizuno et al. 1995) and the Ophiuchus-north region (0.3%; $l = 355^\circ\text{--}12^\circ$, $b = 15^\circ\text{--}23^\circ$; Tachihara et al. 2000). Boulanger et al. (1998) studied Cha II with CO and *IRAS* and reported that the ratio between the mass needed to gravitationally bind the cloud and the gas mass is 7.8, indicating that Cha II is not gravitationally bound. They suggest that Cha II may be two independent clouds not bound together, because the CO spectrum has two lines. Mizuno et al. (1999) mapped Cha II in C^{18}O and combined their work with previous infrared and optical studies of the cloud. They report two velocity components in the C^{18}O for the southeastern part of the cloud and suggest that Cha II and Cha III might be superimposed along the line of sight. Therefore, it is unclear whether Cha II itself is bound. Mizuno et al. (1999) also compared their Cha II results with similar previous work on other molecular clouds, such as Taurus (Onishi et al. 1996) and the Ophiuchus-north region (Tachihara et al. 2000; see Mizuno et al. 1999; Table 2). The mean molecular column density $[N(\text{H}_2)]$ of Cha II, $5.1 \times 10^{21} \text{ cm}^{-2}$, is slightly smaller than that of Ophiuchus-north, $5.9 \times 10^{21} \text{ cm}^{-2}$, or Taurus, $6.9 \times 10^{21} \text{ cm}^{-2}$ (Mizuno et al. 1999; Table 2). Mizuno et al. (1999) also found a

half-power Gaussian line width, ΔV , of 0.78 km s^{-1} in Cha II, which is similar to that in Ophiuchus-north ($\Delta V = 0.7 \text{ km s}^{-1}$) but greater than that of Taurus ($\Delta V = 0.49 \text{ km s}^{-1}$). Mizuno et al. (1999) report that the young stars in Cha II are not densely clustered but are in sparse groups. There is a group of T Tauri stars in the southern tip of the cloud, and other known T Tauri stars are scattered along the eastern edge and to the east of the cloud (Mizuno et al. 1999).

2. OBSERVATIONS

2.1. MIPS Observations

The general *Spitzer* mapping strategy of Cha II was consistent with that of the other four molecular clouds in the c2d Legacy program (Evans et al. 2003). All the area in the Cha II molecular cloud with $A_V > 2$ mag (Cambr sy 1999) was mapped with MIPS (Rieke et al. 2004) on 2004 April 6 (Program ID 176, AOR [astronomical observation request] keys 0005741056, 0005744640, 0005744896, and 0005745152). A total area of over 1.5 deg^2 was mapped in the MIPS fast-scan mode. The fast-scan mode observes in all MIPS wavelength bands (24, 70, and 160 μm) simultaneously. The pixel size is $2''.5$ at 24 μm , $10''$ at 70 μm , and $16'' \times 18''$ at 160 μm . A more detailed description of MIPS can be found in Rieke et al. (2004) or the *Spitzer* Observer's Manual (2004b, pp. 245–348). Cha II was covered by two *Spitzer* AORs, 1° long in the scan direction by 11 scan legs ($0''.7$) and 14 scan legs ($0''.9$) wide. The scan legs were offset from each other by $240''$. Figure 1 shows the 24 μm map of Cha II; the scan direction is approximately east-west. In fast-scan mode, MIPS integrates for 3 s per pointing on the sky. Any individual position

on the sky is observed 5 times at 24 and 70 μm , for an integration time of 15 s per position on the sky. However, the effective 70 μm field of view (FOV) is only half that of the 24 μm array (about $5' \times 5'$), because only one-half of the 70 μm array returns usable data. By design, the 160 μm coverage in fast-scan mode is not complete. The 160 μm array has an FOV of only $0.5' \times 5'$ and is further reduced by a dead readout (Rieke et al. 2004). The integration time at any position on the sky at 160 μm is either 0 or 3 s in fast-scan mode. The integration times are higher in all bands in regions where the scan legs or AORs overlap.

The entire cloud was observed twice. The second observation, or epoch, began about 6 hr after the first. The AORs were designed with a 3–6 hr separation of epochs to enable the detection and removal of asteroids at 24 μm . The two epochs were offset from one another on the sky by about half an array ($125''$) in the cross-scan direction. The offset was designed to fill in the gaps left by the side of the 70 μm array that does not return usable data. This observation strategy results in approximately the same coverage at 24 and 70 μm but less total (two epoch) integration time at 70 μm (15 s) than at 24 μm (30 s). In addition, the second epoch was shifted by $80''$ in the scan direction to partially fill the gaps in the 160 μm coverage area. The 160 μm coverage is still not complete with two observations, but the gaps are minimized.

2.2. SIMBA Observations

Millimeter-continuum observations were made during the period 2001 November 10–15 with the 37-channel bolometer array SIMBA at SEST on La Silla, Chile. We observed two regions that cover the areas of highest optical extinction toward the Cha II complex. The northern region has an approximate extent of $4000'' \times 4000''$, and the southern one has an extent of roughly $2000'' \times 2000''$, for a total coverage of over 1.2 deg^2 . The area mapped by SIMBA is slightly smaller than and fits within the MIPS observation area. SIMBA is sensitive between about 200 and 280 GHz, with an effective frequency of 250 GHz or an effective wavelength of 1.2 mm.

In total, 46 maps were taken in the fast-scanning mapping mode with a scanning speed of $160 \text{ arcsec s}^{-1}$. Each of the maps consists of 89 subscans in azimuth with a length of $1400''$, with $16''$ of spacing in elevation between subscans (and thus a total map extent of $1408''$ in elevation). The pointing uncertainties are of order $7''$ – $16''$, as determined from (and corrected on the basis of) offsets between the SIMBA and MIPS positions of IRAS 12496–7650, while SEST has an HPBW of $24''$ at 250 GHz. The zenith opacity, which was determined by sky dips performed at least every second hour for most of the data (and at least every fifth hour in some cases), ranged from 0.23 to 0.37. Maps of Uranus and Mars were used for calibration purposes. The derived calibration factor of $123 \text{ mJy counts}^{-1}$ is in very good agreement with the factor of $130 \text{ mJy counts}^{-1}$ determined by the telescope crew for this observing period. On the basis of frequent observations of η Carinae, we estimate the relative calibration uncertainty to be within $\pm 15\%$.

3. DATA REDUCTION

3.1. MIPS Data

MIPS images were processed by the *Spitzer* Science Center (SSC) using the standard pipeline (ver. S9.5) to produce Basic Calibrated Data (BCD) images (Gordon et al. 2005; Masci et al. 2005; MIPS Data Handbook 2004a). The BCD images were then further corrected for some instrumental signatures as described below. Other instrumental signatures, e.g., dark latents, column and row pull-down effects, and streaks extending from bright

objects, have not been corrected for. Bright latent images occur at roughly $60''$ intervals in the scan direction after a bright object. No attempt was made to explicitly remove cosmic rays or bright latent images from the BCD images. To avoid misidentifying these as point sources, we used either inspection or the redundancy and outlier rejection in mosaicking. Some of the bright latent images can be seen to the east and west of the bright sources in the 24 μm map of Cha II (Fig. 1). Complete details of the c2d processing are available from the SSC¹³ (Evans et al. 2004).

3.1.1. The 24 μm Fast-Scan Map Data

With the 24 μm array, a jailbar pattern results from bright sources or from cosmic-ray hits. The jailbars are time-dependent variations in the relative gains between readouts in the array. We applied a multiplicative correction to each BCD frame for any detectable fixed-amplitude jailbar pattern across the array, bringing lower columns up to the level of the highest columns. For some data, we corrected the jailbarring in two sections, rows above and rows below a bright object. A few frames had a more complex jailbar pattern, and these were dropped from further analysis. In addition, “first frame” corrections were applied. Scale factors were applied to the first four frames in a map to bring them up to the median of subsequent frames. Finally, frames in each scan leg were median-combined to create “self-flats.” Each frame was divided by the self-flat for that scan leg. This procedure corrected for residual jailbarring and a 1%–2% gradient along the column direction. Uncertainties resulting from these corrections to the pixel values are estimated to be typically $\lesssim 0.2\%$ and the resulting uncertainties in point-source fluxes $\lesssim 0.03 \text{ mJy}$. This uncertainty is small compared to that of other sources.

3.1.2. The 70 and 160 μm Fast-Scan Map Data

The 70 and 160 μm data contain several instrumental signatures. The SSC provided two types of BCD images: normally processed (unfiltered) and those with a time-median filter applied that removes most of the background signal (filtered). Following the current recommendation of the SSC, we used the 70 μm filtered data to obtain point-source fluxes. However, only the unfiltered data preserve extended emission.

We are ultimately interested in fluxes for both point sources and extended emission. In this paper, we present preliminary maps made from unfiltered 70 and 160 μm data. The 70 μm map includes approximate corrections for instrumental effects, as described below. The flux calibration for extended emission in the 70 and 160 μm data is uncertain at the present time. The corrections applied at 70 μm may not lead to properly calibrated data. The maps should be seen as only illustrating rough levels of extended emission.

First, after stimulator (stim) flashes in 70 μm data, there was a “stim latent” signal present in subsequent BCD frames. The first frame after the stim flash was the most affected; the four frames after the stim flash could have some residual effect. We applied a column-by-column subtractive correction based on the level after the latents decayed. Second, the unfiltered data had striped patterns approximately along the column direction due to suspected response variations (on the order of several times 10%). We created an illumination correction made from the data themselves by median-combining frames in each scan leg. However, the corrected data are of uneven quality. Surface brightness uncertainties introduced by these corrections are difficult to estimate without a better understanding of the instrument. However,

¹³ See the documentation at <http://ssc.spitzer.caltech.edu/legacy>.

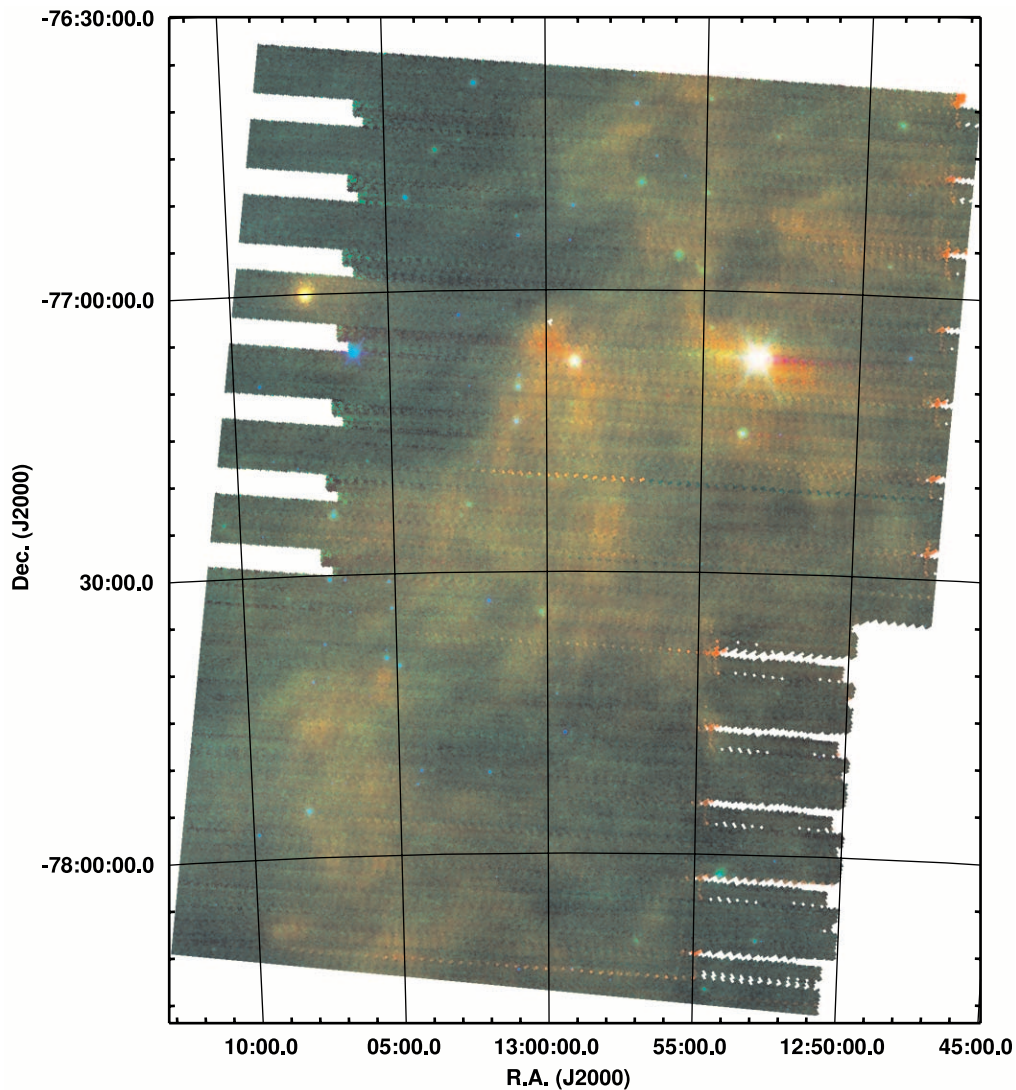


FIG. 2.—Three-color MIPS 24 μm (blue), 70 μm (green), and 160 μm (red) map of the Cha II molecular cloud. The figure has been cropped to include only areas for which there are data at all three wavelengths.

the amplitude of the illumination corrections, several times 10%, may be a rough estimate. No changes were made to 160 μm unfiltered BCD data as the steps needed for extended-source calibration are still in a preliminary stage.

3.1.3. Image Mosaicking

The mosaic images produced for each wavelength are important both for the overview they provide of the mapped area, especially of the diffuse extended emission, and because our source extraction process begins by searching for sources in the mosaics. A three-color (24, 70, and 160 μm) mosaicked image of Cha II is shown in Figure 2. This map shows the unfiltered 70 and 160 μm data to display the extended emission in Cha II. The primary tool for mosaicking is the SSC MOPEX code (Makovoz 2004). This code includes a continuously evolving set of modules that correct for some problems in the BCD and attempt to piece many BCD images together into large mosaics. Optional modules exist to filter out radiation hits (outlier rejection) and to correct for small positional errors in the FITS headers (position refinement).

For the 24 μm data, we have used MOPEX with the outlier rejection and position refinement modules turned on with nom-

inal parameters. To detect asteroids, we have divided the total data set into two separate groups of BCD images, according to the two epochs in which our data were acquired, and processed each independently. The actual process of identifying asteroids and combining the two epochs into a single, higher reliability source list is described later, in § 3.1.5. In total, we construct separate mosaics for each epoch plus a combined mosaic in which the highest signal-to-noise ratio is obtained.

As part of its standard processing, MOPEX makes use of mask files to avoid including in the final mosaic BCD pixels that have been identified as having some problem. For our mosaics, we used a combination of the masks created in the initial c2d processing, together with the outlier masks constructed during the outlier-rejection processing by MOPEX. The masks created by the c2d team effectively combine the bad-pixel masks (“pmask”) and the bad-detection masks (“dmask”) of the SSC.

The geometry of the mosaics constructed with MOPEX for this paper was such that we kept a 1 : 1 pixel size ratio between the basic instrument pixel size and mosaic pixel size, and we assembled the BCD images in a coordinate system essentially fixed with respect to the average instrument rotation projected on the sky. The former minimizes file sizes and processing time.

The latter simplifies the process of point-source extraction from the mosaics, since the instrumental point-spread function (PSF) has the same rotational orientation for any mosaic.

3.1.4. Source Extraction

The process of source extraction involves finding likely compact objects in the data and characterizing them by flux, position, and some estimate of the way in which they might differ from a “perfect” pointlike object. The details of our point-source extractor will be described in a future paper (P. M. Harvey et al. 2005, in preparation), but we summarize the main points here.

The source extraction tool, c2dphot, is based on the venerable DoPHOT code described by Schechter et al. (1993). Our version includes the following important modifications to DoPHOT: (1) it utilizes a digitized point-source profile, rather than an analytic one, to best match the real *Spitzer* data, (2) it accepts floating-point input FITS images and computes output fluxes based on the *Spitzer* surface brightness units in the BCD images, (3) it accepts input masks to avoid using pixels that have been declared bad for whatever reason, and (4) it includes a multi-frame mode that fits fluxes and positions from the entire stack of BCD frames relevant to any input source position using the unsmoothed instrumental PSF rather than that produced by the mosaicking process. The most significant unchanged aspect of c2dphot/DoPHOT is the basic source extraction process. In particular, c2dphot starts at an upper flux level, finds and characterizes sources above that level, and subtracts them from the image. It then works its way down in flux, typically by steps of a factor of 2 each time, doing the same thing until it reaches the lower flux limit input by the user. If c2dphot finds an object that is better fitted by a two-axis ellipsoid than the numerical point-source profile, it classifies the object as extended and produces estimates of the source size and tilt of the ellipse.

Like any source extractor, there are many tunable parameters in c2dphot to enable it to deal with a variety of problems or characteristics in the data. We discuss here the most important and how we tuned them for the sources found in this analysis. The most sensitive parameters for both accurate source extraction and photometry are the sizes of the search box, fitting box, and aperture photometry boxes. For these data, we used search and aperture boxes of 7 pixels and a fitting box of 5 pixels, based on a number of tests on simulated data sets, as well as a variety of real data from *Spitzer*. Other tunable parameters include thresholds for deciding whether a source is extended, whether an initial detection is better fitted by a tilted plane, and whether a source is so small that it is more likely to be a previously undetected radiation hit. These have all been tuned to levels that appear appropriate from careful visual inspections of subsets of the data.

The details of the c2dphot source extraction processing for the 24 μm data involve running the source extractor first on the mosaic image produced by MOPEX. Then the multiframe option is run with the output list from the previous processing given as an input list for flux, position, and shape refinement, but no new source searching is done. As mentioned above, this procedure ensures that the source characteristics are derived from the least processed form of the data, the BCD products. For MIPS 70 μm data we have extracted sources from the mosaics made with the filtered BCD images with c2dphot.

The calibration of source fluxes is done in the following way. For all objects for which a reliable aperture flux could be determined and which were well fitted by the nominal point-source profile, the ratio of the aperture flux to model flux was averaged. The fact that this ratio is not unity is expected since the model fluxes are essentially the product of a single number, the fitted

peak value, multiplied by the PSF area. Small errors and uncertainties in the PSF area then lead to errors in the total model flux. We then assume that this average ratio of aperture flux to model flux applies for all point sources and multiply by an additional correction factor of about a factor of 2 at 24 μm for the aperture used in c2dphot relative to that for the absolute calibration used by the SSC (essentially a traditional aperture correction). This correction introduces absolute flux uncertainties of up to 10%.

Relative flux and position uncertainties in c2dphot are calculated in a standard way from a numerical estimate of the Hessian matrix (Press et al. 1997; Sivia 1996). In particular, the matrix of partial gradients of χ^2 is calculated numerically for variations in the four model parameters (for point sources). This is done by fixing each parameter at levels offset slightly above and below the best-fit parameter and calculating the change in χ^2 for all combinations of offset parameters. The diagonal elements of the square root of the inverse of this matrix then give an error estimate, at least in cases for which the errors are reasonably behaved. A random check of the off-diagonal elements has shown that the only significant correlation between error estimates is that expected between the derived sky level of the fit and the peak star amplitude. For extended extractions a similar procedure is part of DoPHOT and c2dphot using analytic rather than numerical estimates of the derivatives.

The absolute uncertainty in the fluxes is at least 5% at 24 μm , 10% at 70 μm , and 20% at 160 μm , as estimated by the MIPS instrument team (Gordon et al. 2004). However, considering uncertainties introduced by the aperture correction in c2dphot, we estimate the total uncertainty in these data to be closer to 10% at 24 μm and 20% at 70 and 160 μm .

3.1.5. Band Merging

The 24 and 70 μm bands were processed differently in the band-merging stage of the c2d pipeline because the 70 μm band has only one effective epoch of observations. Our observations were planned so that our second epoch would fill in the gaps in the coverage at 70 μm caused by the unusable half of the array.

The final list of sources and fluxes was produced in three steps. First, the source extractions for 24 μm in the two epochs are compared. A source detection in one epoch that has only a single match within 2''0 in the other epoch and no other matches in its own epoch is considered a good source, and the two detections are averaged. Detections that do not have any match within 2''0 in either epoch or detections with more than one match in an epoch are suspect sources, and these are checked to ensure that no valid sources are missed. The candidate sources are then filtered to include only those sources with fluxes greater than or equal to 10 times the flux uncertainty (10σ). Asteroids, which are bright at 24 μm , shift positions between the two epochs. As a result, they are excluded in this step because an asteroid detected in one epoch would not have a corresponding detection within 2''0 in the second epoch. As expected, due to the ecliptic latitude of Cha II of -65° , no asteroids were detected at 24 μm in the data. Asteroids are not bright enough at 70 μm to be detected.

In step two, the filtered source extractions for 24 μm are compared with the source extractions made from the combined-epochs images. A good source detection has only a single match within 2''0 in both the filtered list and the combined-epochs list. For these sources, the position and flux information from the combined-epochs detection is substituted as the best value for the source. As in step 1, sources not detected within 2''0 in both the filtered list and the combined-epochs list or sources containing multiple detections within 2''0 in either list are examined

and saved if saving is merited. The final list of good sources at 24 μm is again filtered to only include those with fluxes greater than or equal to 10σ . Because we only have one epoch of observations at 70 μm , only the sigma-clipping was performed in this step for the 70 μm data.

The 24 and 70 μm bands were merged in step 3. The source extraction program produced many artificial detections near the ends of the MIPS scan legs at 70 μm . Most of these false detections were eliminated from the source list by the 10σ cut and by removing sources with aperture fluxes less than or equal to zero. The final 70 μm source list was then band-merged with the 24 μm source list.

3.2. SIMBA Data

The SIMBA 1 mm mosaics were reduced and combined using the MOPSIC¹⁴ software package. The noise in the maps forces us to subtract correlated sky noise and baselines of order 2, which both filter out emission on large scales. The correlated sky noise was evaluated as a weighted mean of the channels spaced by more than $50''$ from the channel to be corrected. Thus, the response to extended sources (i.e., those with diameter larger than the correlation radius of $50''$) is damped by the sky-noise filter. Such sources are not quantitatively preserved. Compact (i.e., those with diameter less than $50''$) and unresolved sources (i.e., those with diameter less than a beam) are not significantly affected by the filter. In total, seven noisy maps and several subscans with spikes and drifts were not included in the mosaic to improve the noise level and to minimize artifacts. The final on-source integration time is therefore 8.4 hr.

We apply a reduction scheme with three iteration steps, which reduces the filtering of extended emission by sky-noise subtraction. After the first step, regions with significant emission are identified and included in a source model. In the second step, the source model is first subtracted from the deconvolved raw data before sky-noise and baseline removal and then again added to the data before co-adding. This yields a map in which the extended emission is better preserved from spatial filtering by the sky-noise filter, while the impact of baseline removal is not mitigated. The improved map is then used to obtain an improved source model, which then is used in a third and final iteration step to derive the final map. We correct for pointing uncertainties by shifting maps by the offset between the SIMBA and MIPS positions of IRAS 12496–7650 observed for the respective epoch (i.e., by $7''$ – $16''$).

4. RESULTS

4.1. MIPS Source Counts

There were 1532 sources at 24 μm and 41 sources at 70 μm identified with fluxes greater than 10σ . Normal source extraction techniques were not possible on the 160 μm data because the emission is so extended and the coverage was incomplete. However, several bright peaks are seen in the map, and 160 μm aperture fluxes are presented for two sources discussed in § 5. In the mosaics, the median background and rms noise values in the off-cloud regions where structured dust emission is low are 16 and 0.1 MJy sr^{-1} at 24 μm , 6 and 0.8 MJy sr^{-1} at 70 μm , and 30 and 4.5 MJy sr^{-1} at 160 μm , respectively.

To determine approximate completeness limits, we plot two parameters versus source magnitude: cumulative source counts and extracted uncertainty. Figure 3 shows the cumulative source

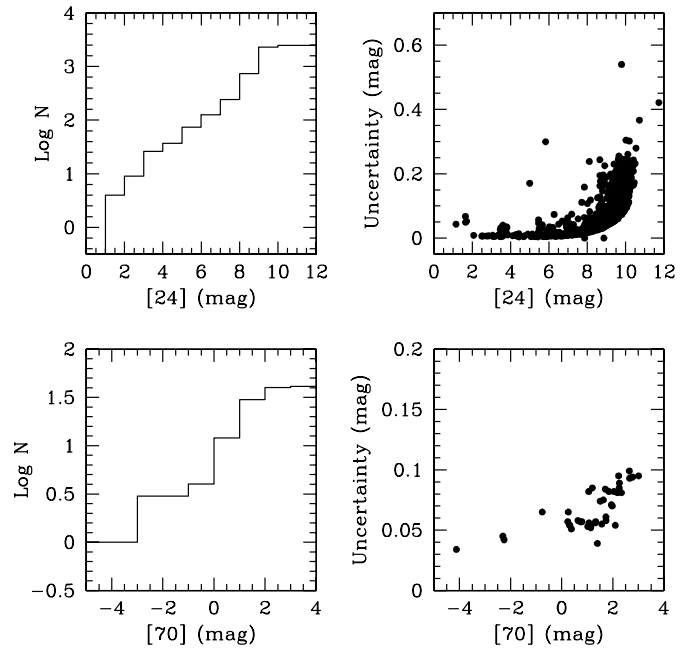


FIG. 3.—*Left*, Logarithm of the cumulative number of counts for 24 μm (*top*) and 70 μm (*bottom*) sources per magnitude bin; *right*, uncertainty of extracted magnitude vs. magnitude for 24 μm (*top*) and 70 μm (*bottom*) sources. The 24 μm counts include all sources extracted from the Cha II map (2481 sources). The 70 μm counts represent only sources that have fluxes greater than 10σ and that are identified as real by eye (41 sources). The estimated completeness from these plots at 24 and 70 μm is 10 mag (0.7 mJy) and 3 mag (50 mJy), respectively.

counts for 24 and 70 μm in Cha II. The 24 μm counts include all sources extracted from the mosaic with no sigma cut (2481 sources). The 70 μm cumulative source counts only include greater than 10σ sources verified by eye to be real (41 sources), since the source extraction produced many artificial detections at the end of the scan legs in this band. The 24 and 70 μm magnitudes were calculated using zero-point fluxes derived from a blackbody corresponding to Vega (Table 1). The source counts flatten at the faintest magnitudes, indicating completeness to about 10 mag (0.7 mJy) at 24 μm and 3 mag (50 mJy) at 70 μm . Plots of magnitude uncertainty versus magnitude for Cha II (Fig. 3) show that the uncertainty reaches 0.1 mag at close to the same values as the turnover in source counts, 10 mag at 24 μm and 3 mag at 70 μm . Experience with other large surveys suggests that 0.1 mag uncertainty is usually about where the 90% completeness level lies. The 24 μm flux limit of 0.7 mJy is consistent with the 3σ sensitivity (0.83 mJy for 24 s integration) predicted for the c2d program by Evans et al. (2003). However, the 70 μm limit of 50 mJy is much higher than the 10σ sensitivity predicted prior to launch (17 mJy in 24 s; Evans et al. 2003), partially due to the loss of half the array and the resultant cut in the integration time. The observed completeness limits are about 5 and 6 times the SSC expected postlaunch 1σ sensitivities with low background and appropriate integration times at 24 and 70 μm , respectively (*Spitzer* Observer’s Manual 2004b).

TABLE 1
ZERO-POINT FLUXES

λ (μm)	$S_\nu(0)$ (Jy)
24.....	7.24
70.....	0.81

¹⁴ MOPSIC is a software package for infrared, millimeter, and radio data reduction and analysis developed and constantly upgraded by R. Zylka.

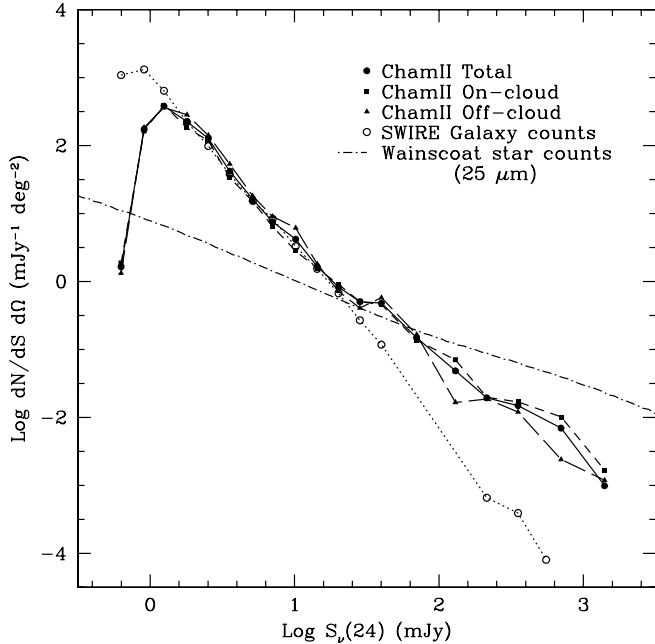


FIG. 4.—Source counts in the Cha II MIPS field. On-cloud counts refer to the area of the map with $A_V > 1$. Off-cloud counts are those in the area where $A_V < 1$. The SWIRE galaxy counts are from Marleau et al. (2004). The dot-dashed line shows the model star counts at $25 \mu\text{m}$ for the latitude, longitude, and distance of Cha II with $A_V = 2$ from Wainscoat et al. (1992). These source counts are consistent with the galaxy counts for $24 \mu\text{m}$ fluxes less than 20 mJy. However, brighter sources are likely Galactic.

Figure 4 shows the $24 \mu\text{m}$ source counts deg^{-2} versus flux [$dN/dS d\Omega$ vs. $S_\nu(24)$] for the total 1532 sources in the complete mosaic of Cha II. The sample is flux limited as shown in Figure 4 by the steep drop in $dN/dS d\Omega$ for $S_\nu(24) < 0.7$ mJy. The complete field can be divided into two regions: on-cloud and off-cloud. The on-cloud field is defined as the area that encloses the Cambr sy (1999) $A_V = 1$ contour and includes 825 $24 \mu\text{m}$ sources. The remainder of the field is considered off-cloud. Figure 4 compares $dN/dS d\Omega$ of the total field (on-cloud and off-cloud samples) with galaxy counts from the *Spitzer* Wide-area Infrared Extragalactic Survey (SWIRE) Legacy project (Lonsdale et al. 2003; Marleau et al. 2004) and model star counts for the position of Cha II at $25 \mu\text{m}$ from Wainscoat et al. (1992). The Wainscoat star counts were computed using a C-version of the model provided by J. Carpenter (2001, private communication). This version of the model allows for the inclusion of extinction in calculating the source counts. The A_V was set to 2 mag as an approximate average between the off-cloud region, where $A_V < 1$, and the on-cloud region, where $A_V = 1-6$ with a few patches of $A_V > 6$ (Fig. 1).

For $S_\nu(24) < 20$ mJy, the Cha II source counts are consistent with the SWIRE galaxy counts. For fluxes greater than about 20 mJy, the Cha II and model star counts exceed the galaxy counts. Therefore, most of the bright $24 \mu\text{m}$ sources are likely associated with the Cha II cloud or are Galactic, while most of the fainter sources are probably galaxies. The Wainscoat et al. (1992) model star counts also exceed the Cha II source counts for $S_\nu(24) > 70$ mJy. Even though the total source and model counts are small in these flux bins, we assume that not all the Cha II sources are background stars. The discrepancy between the Wainscoat model and the data appears real and indicates that the model overestimates the star counts toward Cha II. Increasing A_V in the Wainscoat model reduces the inconsistency. However, an A_V value of 20 mag is

needed for the model counts to be approximately equal to the total source counts for bright sources. This large extinction is only seen for a few isolated positions in the cloud, so it is not the best choice for the model. For $24 \mu\text{m}$ fluxes greater than 70 mJy, there is an excess of on-cloud sources over off-cloud sources (21 on-cloud vs. 7 off-cloud). Although this excess is statistically small, the numbers are representative of the locations of previously known YSOs in Cha II. There are a small number of T Tauri-type stars associated with Cha II in the off-cloud ($A_V < 1$) area. Figure 1 shows the *Spitzer* $24 \mu\text{m}$ map of Cha II with A_V contours and known and candidate YSOs marked. This figure shows that most of the YSOs in Cha II are on the eastern edge of the cloud rather than in areas of high extinction.

4.2. MIPS-2MASS Color-Magnitude Diagrams

The $24 \mu\text{m}$ source list was band-merged with the Two Micron All Sky Survey (2MASS) catalog (Cutri et al. 2003) for matches within $2''.0$. We identified 626 sources that have both a $24 \mu\text{m}$ and K_s ($2.159 \mu\text{m}$) detection. The magnitude limit of the 2MASS catalog is $K_s \sim 15$ mag. These sources are plotted in a K_s magnitude versus $K_s - [24]$ color diagram in Figure 5. The diagonal cutoff at lower left of the figure indicates the $24 \mu\text{m}$ flux limit of around 0.7 mJy. Two large clusters are seen in the plot. The first clump, at $K_s - [24] = 0$, contains main-sequence stars. The second cluster, at $K_s > 13$ mag and $K_s - [24] > 4$ mag, probably consists mainly of galaxies. Using data from the SWIRE extragalactic survey with *Spitzer* (Lonsdale et al. 2003; Surace et al. 2004), we predict where galaxies are likely to fall in the K_s versus $K_s - [24]$ color-magnitude space. Most of the SWIRE galaxies fall between $K_s - [24] = 4.5$ and 8.5 mag with $K_s > 13$ mag, indicated by a box in Figure 5. A few SWIRE objects trail out between $K_s - [24] = 3$ and 4.5 mag, all those with $K_s > 12$ mag,

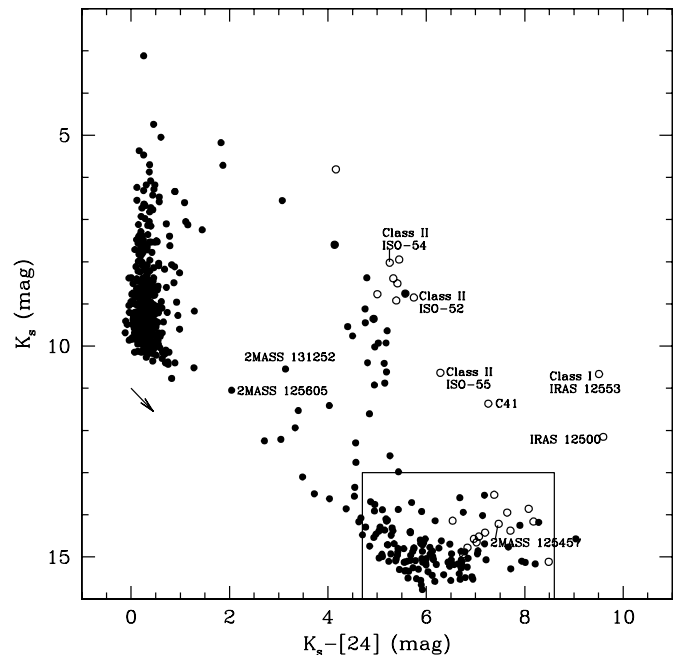


FIG. 5.—Color-magnitude diagram for the 2MASS K_s -band and the MIPS $24 \mu\text{m}$ -band sources in Cha II. Of the $24 \mu\text{m}$ MIPS sources in Cha II 626 (41%) have K_s detections. Sources with $70 \mu\text{m}$ detections are shown by open circles. The box denotes where the SWIRE galaxies would fall on this plot. Known Class I and II sources from Persi et al. (2003) and sources described in § 5 are labeled. The arrow shows the reddening vector for $A_V = 5$ mag using the Weingartner & Draine (2001) dust model with $R_V = 5.5$. Sources with $K_s < 13$ mag and $K_s - [24] > 1$ are considered YSO candidates.

TABLE 2
YSOs AND YSO CANDIDATES IN CHA II

c2d Name	Other Name(s)	R.A. (J2000.0) ^a	Decl. (J2000.0) ^a	24 μm^b (mJy)	σ	70 μm^b (mJy)	σ	$\alpha_{24/K}$	Reference
SSTe2d J124505.8–772014	IRAS 12416–7703	12 45 07.0	–77 20 13.8	1590	100	102	8.3	–1.29	1
SSTe2d J124825.7–770637	IRAS 12448–7650	12 48 25.6	–77 06 36.9	331	2.8	–2.18	2
SSTe2d J125217.2–780038	IRAS F12486–7744	12 52 17.5	–78 00 37.4	29.6	0.23	–2.44	2
SSTe2d J125230.6–771513	IRAS F12488–7658/C13	12 52 30.5	–77 15 13.3	34.7	0.20	–2.33	3
SSTe2d J125342.8–771512	IRAS 12500–7658	12 53 42.6	–77 15 10.3	687	4.2	1630	100	0.79	2
SSTe2d J125605.5–765411	2MASS 12560549–7654106	12 56 05.2	–76 54 10.6	1.81	0.09	–2.10	4
SSTe2d J125633.6–764545	Sz 46N	12 56 33.6	–76 45 45.6	57.1	0.28	–1.16	5
SSTe2d J125658.7–764707	Sz 47	12 56 58.5	–76 47 07.2	1.11	0.07	–1.84	5
SSTe2d J125711.7–764011	IRAS 12535–7623/CHIXR2	12 57 11.5	–76 40 10.5	430	3.5	147	12	–0.84	2
SSTe2d J125806.8–770909	ISO-Cha II-13	12 58 06.7	–77 09 09.6	8.39	0.14	–0.87	6
SSTe2d J125906.6–770740	IRAS 12553–7651/ISO-Cha II-28	12 59 06.4	–77 07 40.0	2500	100	6720	290	0.76	6
SSTe2d J125909.7–765104	C41	12 59 10.4	–76 51 03.1	165	1.2	123	9.7	–0.10	3
SSTe2d J125926.4–774709	IRAS 12556–7731	12 59 26.3	–77 47 08.8	294	1.2	–1.70	2
SSTe2d J130053.1–765416	ISO-Cha II-55/Sz 49/CHIXR9	13 00 53.2	–76 54 14.9	132	0.86	131	8.8	–0.47	6
SSTe2d J130053.3–770909	ISO-Cha II-51/Sz 48/CHIXR7	13 00 53.4	–77 09 08.9	96.6	0.40	–1.06	6
SSTe2d J130055.3–771022	ISO-Cha II-52/Sz 50/CHIXR8	13 00 55.5	–77 10 20.3	416	2.2	604	31	–0.68	6
SSTe2d J130059.3–771403	ISO-Cha II-54/CHIXR10/C48	13 00 59.5	–77 14 03.1	566	3.4	288	15	–0.87	6, 3
SSTe2d J130158.9–775122	Sz 51	13 01 58.4	–77 51 19.9	123	0.57	109	8.4	–0.99	5
SSTe2d J130213.5–763758	IRAS 12584–7621/CM Cha	13 02 13.9	–76 37 57.8	416	2.1	411	22	–0.81	2
SSTe2d J130222.8–773449	C50	13 02 22.8	–77 34 49.7	8.07	0.10	–1.34	3
SSTe2d J130247.5–770240	IRAS 12589–7646	13 02 47.6	–77 02 40.1	209	2.0	–2.16	2
SSTe2d J130423.9–765002	Hn 23	13 04 23.6	–76 50 03.3	226	4.1	448	24	–0.96	5
SSTe2d J130424.9–775230	Sz 52	13 04 24.9	–77 52 30.6	49.0	0.1	–0.89	5
SSTe2d J130455.7–773950	Hn 24	13 04 55.9	–77 39 49.5	280	1.9	243	13	–0.82	5
SSTe2d J130508.5–773343	Hn 25/C53	13 05 08.4	–77 33 42.9	79.0	0.90	–0.96	3, 5
SSTe2d J130512.7–773052	Sz 53	13 05 12.5	–77 30 52.9	91.6	0.66	–0.90	5
SSTe2d J130520.6–773902	Sz 54	13 05 20.8	–77 39 00.9	299	1.4	284	14	–1.30	5
SSTe2d J130630.3–773401	Sz 55	13 06 30.4	–77 34 00.4	29.4	0.21	–0.99	5
SSTe2d J130638.5–773036	Sz 56	13 06 38.7	–77 30 35.6	56.7	0.22	–0.91	5
SSTe2d J130656.5–772310	Sz 57/C60	13 06 56.5	–77 23 09.7	36.7	0.17	–1.33	3, 5
SSTe2d J130657.4–772342	IRAS 13030–7707/C61/Sz 58	13 06 57.2	–77 23 39.6	386	1.9	636	39	–0.75	3
SSTe2d J130709.0–773031	Sz 59	13 07 09.1	–77 30 30.7	265	1.5	–1.05	5
SSTe2d J130718.0–774053	C62	13 07 18.0	–77 40 53.2	14.3	0.10	–1.02	3
SSTe2d J130722.8–773724	Sz 60	13 07 22.4	–77 37 22.6	63.8	0.74	–1.19	5
SSTe2d J130748.5–774121	Hn 26	13 07 48.4	–77 41 21.7	68.1	0.27	–0.98	5
SSTe2d J130806.2–775505	Sz 61	13 08 06.4	–77 55 04.9	724	4.2	572	27	–0.79	5
SSTe2d J130827.2–774323	C66	13 08 27.2	–77 43 23.5	5.85	0.09	–1.13	3
SSTe2d J130910.3–770944	IRAS F13052–7653/CHIXR60	13 09 09.9	–77 09 43.8	122	1.6	–0.89	2
SSTe2d J130950.3–775724	Sz 62	13 09 50.3	–77 57 24.3	130	0.88	–1.06	5
SSTe2d J131004.3–771045	Sz 63	13 10 04.2	–77 10 44.9	42.1	1.1	–1.04	5
SSTe2d J131025.3–772909	2MASS 13102531–7729085	13 10 25.3	–77 29 08.6	3.84	0.10	–1.13	4
SSTe2d J131103.3–765333	2MASS 13110329–7653330	13 11 03.3	–76 53 33.1	1.56	0.11	–1.71	4
SSTe2d J131252.3–773918	2MASS 13125238–7739182	13 12 52.3	–77 39 18.1	7.89	0.08	–1.68	4
SSTe2d J131403.5–775308	Sz 64	13 14 03.6	–77 53 07.9	37.2	0.18	–0.91	5

NOTE.—Units of right ascension are hours, minutes, and seconds, and units of declination are degrees, arcminutes, and arcseconds.

^a Positions are from the 24 μm map.

^b The flux uncertainty σ is calculated using c2dphot as described in § 3.1.4. The absolute uncertainty in the flux is closer to 10% at 24 μm and 20% at 70 μm .

REFERENCES.—(1) Gauvin & Strom 1992; (2) Prusti et al. 1992; (3) Vuong et al. 2001; (4) this work; (5) Chen et al. 1997; (6) Persi et al. 2003.

indicating that some of the sources in the plot that are faint at K_s but have $K_s - [24] < 4.5$ might also be galaxies. However, 5 of the 11 sources with $11 \text{ mag} < K_s < 13 \text{ mag}$ and $K_s - [24] < 5.5 \text{ mag}$ were identified as YSO candidates by Vuong et al. (2001) or Persi et al. (2003). Therefore, that region of color-magnitude space is ambiguous.

Reddened sources with relatively bright K_s magnitudes between the star and galaxy clusters in the K_s vs. $K_s - [24]$ plot (Fig. 5) are potential YSOs associated with Cha II. Class II sources fall in the middle of the plot, with bright K_s magnitudes and red $K_s - [24]$ colors. The Class I sources IRAS 12553–7651 (ISO-Cha II-28; Persi et al. 2003) and IRAS 12500–7658 (Chen

et al. 1997) are outliers, with the reddest $K_s - [24]$ colors. To find potential YSOs, we identified sources with $K_s < 13 \text{ mag}$ and $K_s - [24] > 1 \text{ mag}$. These criteria eliminate galaxies and stars but also generally exclude Class III sources, which have colors similar to stars. Forty-nine sources fit these criteria and were cross-checked with known YSOs from the literature. Forty were previously identified as YSOs or YSO candidates (Gauvin & Strom 1992; Prusti et al. 1992; Chen et al. 1997; Vuong et al. 2001; Persi et al. 2003). Five of the sources have spectral energy distributions (SEDs) consistent with those of highly extinguished background stars. Two sources are possible YSOs but are very faint at K_s ($> 12 \text{ mag}$) and cannot be distinguished from galaxies with these

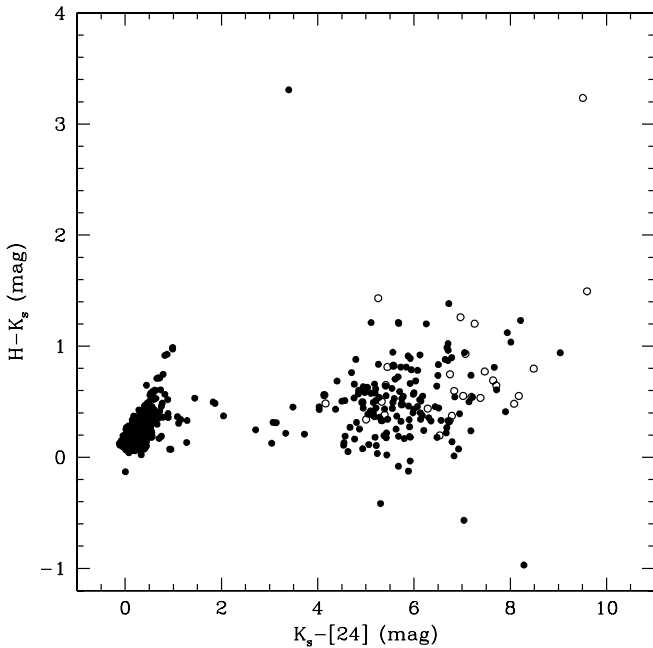


FIG. 6.—Color-color diagram comparing 2MASS $H - K_s$ vs. $K_s - [24]$, showing sources with $70 \mu\text{m}$ detections (open circles). Sources with $K_s - [24] > 3$ mag cannot be distinguished from galaxies in this color-color space.

data. However, the SEDs of two sources (2MASS 12560549–7654106 and 2MASS 13125238–7739182) indicate that they have a $24 \mu\text{m}$ excess and are likely stars with disks. These sources are described further in § 5. The 40 previously identified and four new YSO candidates selected from the color-magnitude diagram are listed in Table 2. This list of YSO candidates includes six identified by Persi et al. (2003, their Tables 3 and 4) with *ISO*, including one of their new candidate YSOs ISO-Cha II-13. Our YSO criteria were unable to identify the Class III sources from Persi et al. (2003), and we did not detect the three other new candidates from their Table 4 with MIPS. Table 2 also includes nine low-mass T Tauri or young brown dwarf candidates identified by Vuong et al. (2001).

Despite the improved sensitivity of MIPS over previous infrared instruments, the small number of new YSO candidates found with MIPS and 2MASS data in Figure 5 indicates that previous studies (e.g., Schwartz 1977; Gauvin & Strom 1992; Prusti et al. 1992; Persi et al. 2003) achieved a nearly complete census of the YSOs in Cha II. However, a later paper will combine the MIPS and IRAC data of Cha II. The IRAC data may allow the identification of more new low-luminosity YSOs among the sources that cannot be distinguished from galaxies with MIPS and 2MASS data alone.

Figure 6 plots $H - K_s$ versus $K_s - [24]$. In this color-color space, the SWIRE (Lonsdale et al. 2003; Surace et al. 2004) galaxies fill nearly the same area as the data with $K_s - [24] > 3$ mag. Therefore, it is very difficult to use this color-color space to identify potential YSOs. A future paper on IRAC observations of Cha II by the c2d team (A. Porras et al. 2005, in preparation) explores different color-color spaces including the IRAC bands for identifying YSOs.

A MIPS 24 and $70 \mu\text{m}$ color-magnitude diagram is shown in Figure 7. Thirty-eight Cha II sources with detections at both 24 and $70 \mu\text{m}$ are distributed in two clumps on the color-magnitude plot, the first with $[24] < 5$ mag and the second with $[24] > 6$ mag. Known Class I and II sources from Persi et al. (2003), as well as some other interesting objects, are labeled on the plot. The

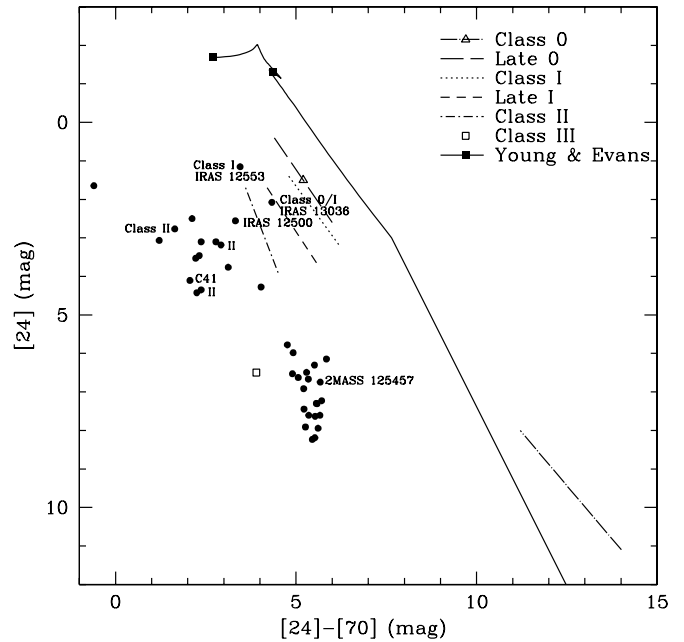


FIG. 7.—Color-magnitude plot of $[24]$ vs. $[24] - [70]$. Model predictions for a low-mass protostar from Whitney et al. (2003, their Fig. 8a) are plotted as lines for Class 0–II and as an open square for Class III. The lines span differences in inclination angle with edge-on at the faint end and are for an aperture size of 1000 AU. The solid line shows an evolutionary track for a $1 M_{\odot}$ protostar from Young & Evans (2005). The filled squares indicate transition points in the Young & Evans model between Class 0–I and Class I–II. Known Class I and II sources (Persi et al. 2003) and selected sources described in the text are labeled and are generally bluer than predicted by the models.

Class II sources fall within the main cluster of sources near $[24] - [70] = 2$ mag. Three Class 0 or I sources, IRAS 13036–7644 (in an isolated core to the east of the main cloud, BHR 86; Bourke et al. 1995; Mardones et al. 1997), IRAS 12553 (Persi et al. 2003), and IRAS 12500 (Chen et al. 1997), fall to the right of the group with redder $[24] - [70]$ colors. All the sources in the second group, with $[24] > 6$ mag, are very faint (> 13 mag) or are not detected at K_s . Since the SWIRE galaxies all have similarly faint K_s magnitudes, the sources in the second group cannot be distinguished from galaxies. The separation between the groups in Figure 7 also suggests that objects brighter than 6 mag at $24 \mu\text{m}$ are likely within the Galaxy.

Models of $1 L_{\odot}$ Class 0–III protostars from Whitney et al. (2003; see their Fig. 8a) and an evolutionary track of a $1 M_{\odot}$ protostar from 4000 to 210,000 yr (Class 0 and I stages; Young & Evans 2005, their Fig. 20) are also plotted on Figure 7. Each Whitney et al. (2003) line on the plot represents a range of inclination angles for a model of a particular class of object observed with a 1000 AU radius aperture. This aperture would be roughly equivalent to a diameter of four $24 \mu\text{m}$ pixels or two $70 \mu\text{m}$ pixels for the distance of Cha II. Young & Evans (2005) also give evolutionary tracks for 0.3 and $3 M_{\odot}$ protostars, but these do not vary significantly from the $1 M_{\odot}$ track, except that the $0.3 M_{\odot}$ track drops down to $[24] \approx 0$ mag for $[24] - [70] < 4$ mag. Most of the Cha II sources with bright $24 \mu\text{m}$ magnitudes have bluer $[24] - [70]$ colors than those predicted either by Whitney et al. (2003) or by the evolutionary track of Young & Evans (2005). However, the Young & Evans (2005) evolutionary track and most of the Whitney et al. (2003) models are for younger protostars (Class 0–I), while Cha II has only a few Class I sources. The Cha II sample is dominated by more evolved Class II objects. The second group of sources, with $[24] > 6$ mag, falls to the right

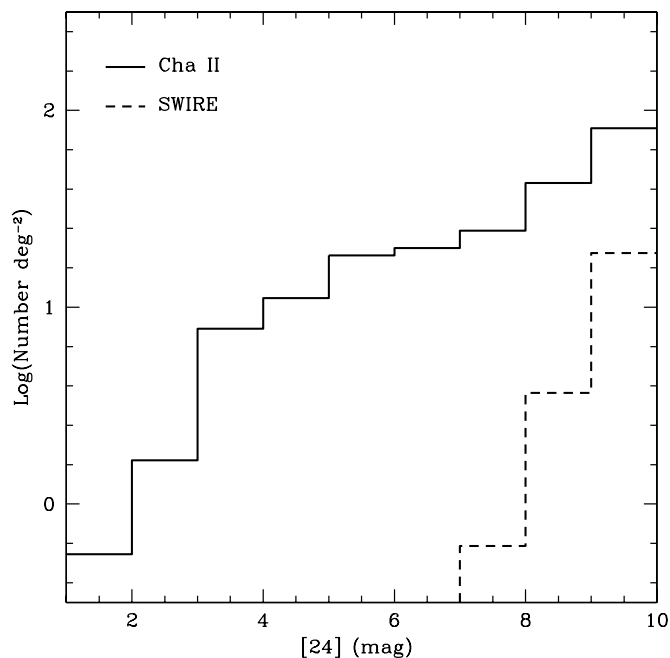


FIG. 8.—Histogram of the logarithm of the cumulative $24\ \mu\text{m}$ source counts deg^{-2} for Cha II (solid line) and the SWIRE extragalactic survey (dashed line) for sources with $1\ \text{mag} < K_s - [24] < 6\ \text{mag}$. Sources brighter than $7\ \text{mag}$ at $24\ \mu\text{m}$ are not likely to be extragalactic.

(greater $[24] - [70]$ color) of the Whitney et al. (2003) prediction for Class III sources, but these sources cannot be distinguished from galaxies with these data alone.

Figure 8 compares the cumulative $24\ \mu\text{m}$ source counts deg^{-2} found in Cha II with those in the SWIRE survey (Lonsdale et al. 2003; Surace et al. 2004). The histogram is limited to sources with $1 < K_s - [24] < 6$ to eliminate background stars. The plot confirms that objects that are bright at $24\ \mu\text{m}$ are not likely to be extragalactic. The Cha II source counts dominate the SWIRE counts for all $24\ \mu\text{m}$ sources brighter than $8\text{--}9\ \text{mag}$, and essentially no galaxies are expected to be detected with magnitudes less than 7.

4.3. MIPS-2MASS Spectral Index

The spectral index for each source with $24\ \mu\text{m}$ and K_s detections was computed according to the equation

$$\alpha_{24/K} = \frac{\log\{[24S_\lambda(24)]/[2.159S_\lambda(K_s)]\}}{\log(24/2.159)}. \quad (1)$$

A histogram of the spectral indices is shown in Figure 9. The figure does not include sources with $K_s > 13\ \text{mag}$ to eliminate as much confusion from galaxies as possible. The figure shows the histograms for on-cloud and off-cloud sources as defined above for the plot of source counts (Fig. 4). Most of the sources (90%) have a spectral index less than -2.5 , with an average of -2.8 , which is consistent with that of main-sequence stars. For clarity, the first bin of the histogram, $\alpha_{24/K} < -2.5$, is not shown to its full extent. There are 233 on-cloud sources and 194 off-cloud sources in the first bin. Lada (1987) defined a near-infrared spectral index for wavelengths from 2 to $20\ \mu\text{m}$ and used it to define boundaries for the class system of YSO classification. According to Lada (1987), a spectral index greater than zero indicates a Class I source, $-2 < \alpha \leq 0$ indicates a Class II, and $-3 < \alpha < -2$ indicates a Class III. Forty-nine (10%) of the sources have $-2.5 < \alpha_{24/K} < 1$, indicating that these sources are possible Class I–III YSOs according to the Lada (1987) clas-

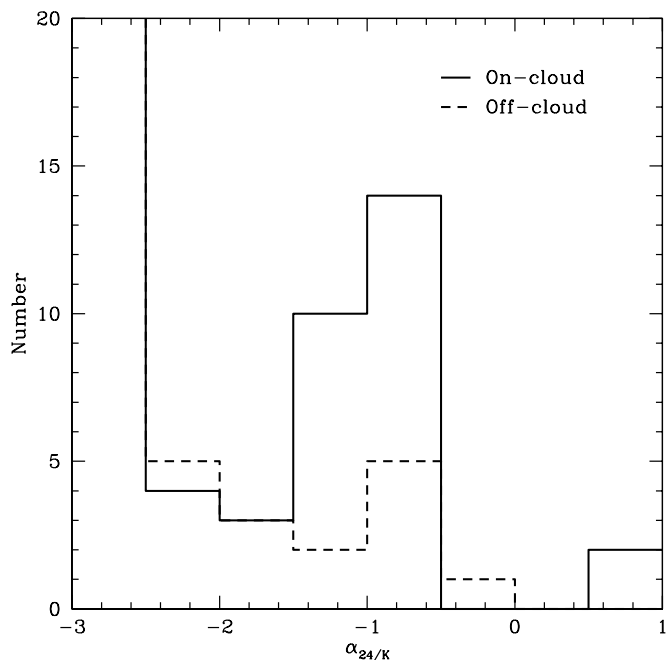


FIG. 9.—Histogram of spectral indices ($\alpha_{24/K}$; Lada 1987) of sources detected at K_s and $24\ \mu\text{m}$ with $K_s < 13\ \text{mag}$, showing on-cloud sources as defined in the text (solid histogram) and off-cloud sources (dashed histogram). The $\alpha_{24/K} < -2.5$ bin continues up to include 233 on-cloud sources and 194 off-cloud sources. Sources with $\alpha_{24/K} > -2.5$ are potential YSOs.

sification. These 49 are the same sources identified as potential YSOs in the K_s versus $K_s - [24]$ plot (Fig. 5), as described above. Two sources, IRAS 12500 and IRAS 12553, both previously classified as Class I protostars (see § 5), have $\alpha_{24/K} > 0$. Both the on-cloud and off-cloud regions contain sources with $\alpha_{24/K} > -2.5$. This is not surprising since there are known T Tauri stars outside the $A_V = 1$ contour used to define the on-cloud region (Fig. 1). The spectral indices of the 44 YSO candidates identified in the K_s versus $K_s - [24]$ plot are listed in Table 2. Figure 1 shows the location of the sources in Table 2 with different symbols indicating their spectral index classification.

4.4. MIPS Extended Emission

Figure 10 shows the MIPS $160\ \mu\text{m}$ contours of Cha II overlaid on a Digital Sky Survey (DSS) R image of the region. The overall shape of the Cha II cloud is outlined well at both wavelengths. The MIPS $160\ \mu\text{m}$ contours reveal details about the shape of the dense cores surrounding the bright *IRAS* sources, IRAS 12496–7650 (DK Cha, an Ae star) and IRAS 12553, at the center of the cloud. The small peak to the east of the main Cha II cloud is BHR 86, a dense core known to be harboring protostars (IRAS 13036–7644; Lehtinen & Higdón 2003). The orientation of the MIPS observations allowed BHR 86 to be observed with Cha II. However, BHR 86 was also the focus of targeted observations by the c2d team with IRAC and MIPS and will be discussed in detail in a future paper. The $160\ \mu\text{m}$ contours also show gaps in the extended emission in the northern part of the cloud, creating ringlike structures. The most pronounced ring in the northeast, near $\alpha = 12^{\text{h}}55^{\text{m}}$, $\delta = -76^{\circ}45'$, contains two classical T Tauri stars (Sz 46N and Sz 47; Chen et al. 1997). Therefore, outflows from these objects may have contributed to the formation of the ring structure. Another prominent feature in the extended emission is the gap at $\delta = -77^{\circ}37'$ separating Cha II into two regions. A group of T Tauri stars lies on the eastern

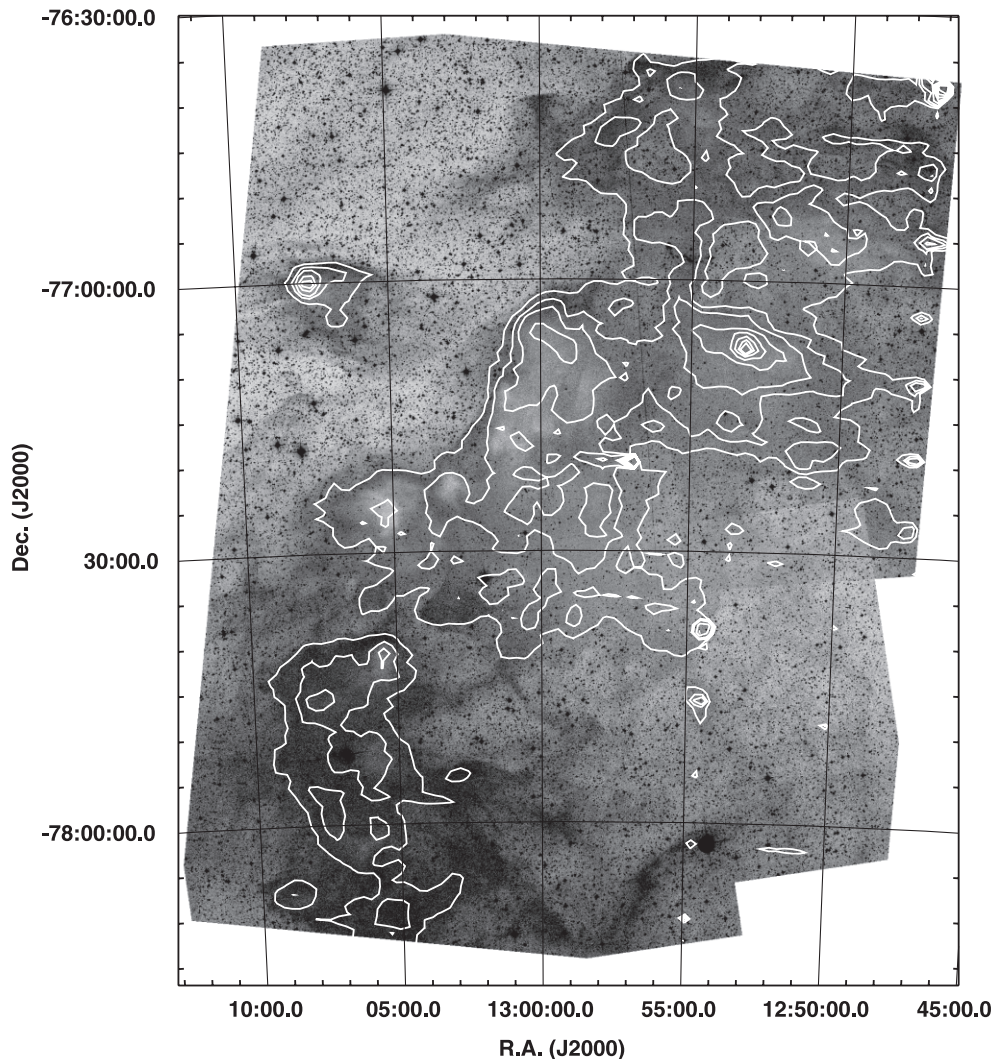


FIG. 10.—Gray-scale DSS R image of Cha II overlaid with MIPS $160\ \mu\text{m}$ contours. Contour levels are 2, 2.5, and 3–8 mJy arcsec^{-2} increasing by $1\ \text{mJy arcsec}^{-2}$. The small round contours on the right edge are caused by noisy ends of MIPS scan legs. From east to west, the peaks are IRAS 13036/BHR 86 ($\alpha = 13^{\text{h}}7^{\text{m}}, \delta = -77^{\circ}$), IRAS 12553 ($\alpha = 13^{\text{h}}, \delta = -77^{\circ}7'$), and IRAS 12496 ($\alpha = 12^{\text{h}}53^{\text{m}}, \delta = -77^{\circ}7'$).

edge of the cloud near the declination of the gap (see Fig. 1), again suggesting that material may have been blown out of this area by forming stars.

The MIPS $160\ \mu\text{m}$ map of Cha II was also compared to the C^{18}O ($J = 1-0$) contours of Mizuno et al. (1999). The peaks in the $160\ \mu\text{m}$ emission are well matched by the peaks of C^{18}O , especially near IRAS 12496 and IRAS 12553. The C^{18}O map, like the $160\ \mu\text{m}$ emission, shows a gap in the cloud near $\delta = -77^{\circ}37'$. There is a hint of the ringlike structures visible in the northern part of the MIPS map in the C^{18}O contours, but they are not easy to distinguish.

4.5. SIMBA Results

Figure 11 shows the dust-continuum emission of the Cha II complex observed by SIMBA. The rms noise level is $32\ \text{mJy beam}^{-1}$ in the center of the map, and toward half the mapped area the noise level is below $70\ \text{mJy beam}^{-1}$. Emission at a significant level ($S/N > 3$) is only detected toward the regions associated with IRAS 12496 and IRAS 12553.

We identify the unresolved source at the highest intensity peak in the millimeter dust emission maps ($694 \pm 42\ \text{mJy beam}^{-1}$) with IRAS 12496; the MIPS data show no other bright nearby

sources. The diffuse, second highest peak in the millimeter-continuum maps ($391 \pm 48\ \text{mJy beam}^{-1}$) is near IRAS 12553 but is offset from its MIPS position by $18''$. This offset appears to be marginally significant when compared to the pointing errors toward IRAS 12496. However, we cannot exclude the possibility that the scans toward IRAS 12553 suffer from additional pointing errors. We therefore identify the millimeter peak with IRAS 12553, as there are no other bright nearby MIPS sources. Table 3 lists the 1 mm fluxes for several MIPS point sources that we discuss in § 5 below, as well as IRAS 12496. The fluxes were derived by integration over an aperture of $80''$ diameter; the listed uncertainties reflect statistical noise. Possible pointing errors would not significantly affect these fluxes, as the aperture is significantly larger than the expected errors. The integrated flux derived for IRAS 12553 is only marginally affected by the uncertain source position and drops by $220\ \text{mJy}$ when the aperture is centered on the millimeter peak. Surprisingly, IRAS 12553 was not detected in the millimeter observations by Henning et al. (1993). Even when taking the extended emission surrounding IRAS 12553 into account, their chopped observations should have detected a source. No obvious explanation for the differences in the inferred fluxes exists.

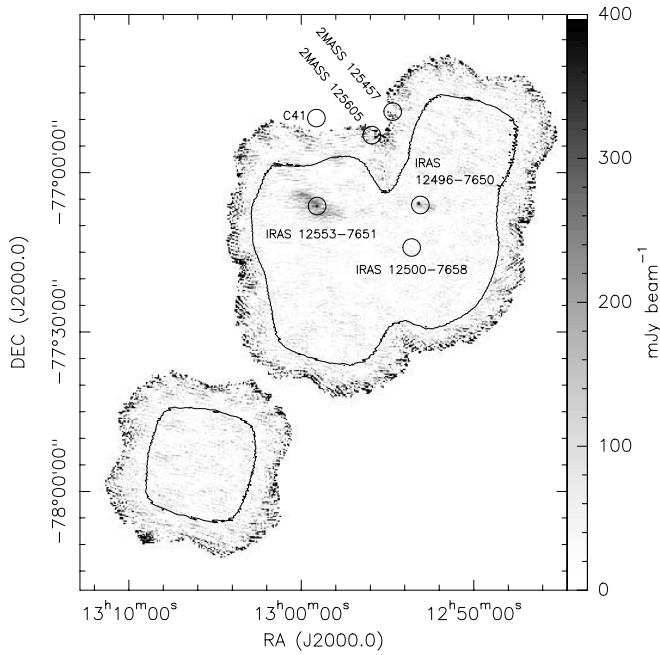


FIG. 11.—Dust-continuum emission map at 1.2 mm of the Cha II complex as observed by SIMBA. The contour delimits the area mapped with an rms noise level below 70 mJy beam⁻¹. The circles are centered on the positions of the MIPS sources discussed in detail in the text. Emission at a significant level is only detected in the regions associated with IRAS 12496 and IRAS 12553.

Extended emission is found west of IRAS 12496 with a total flux of 3.4 ± 0.3 Jy and surrounding IRAS 12553 with 35 ± 1 Jy. Assuming a dust temperature of 10 K and a dust opacity of $0.01 \text{ cm}^2 \text{ g}^{-1}$ at a wavelength of 1.2 mm (Ossenkopf & Henning 1994; we assume a gas-to-dust ratio of 100), we derive a gas mass of $6.5 \pm 0.6 M_{\odot}$ for the extended gas associated with IRAS 12496 and a mass of $67 \pm 2 M_{\odot}$ for the gas associated with IRAS 12553. We identify these extended features with the C¹⁸O cores 14 (for the region close to IRAS 12496) and 19 (for IRAS 12553) found by Mizuno et al. (1999), for which they quote masses of 36 and $64 M_{\odot}$, respectively. While for the extended gas toward IRAS 12553 the mass derived from the continuum emission and the mass derived from C¹⁸O agree, there is a significant difference between the mass estimates for the extended gas near IRAS 12496. The different mass recovery fractions could be due to the effect of spatial filtering. If the gas near IRAS 12553 is in more compact structures than the gas near IRAS 12496, then a larger fraction of its mass would be recovered; gas significantly more extended than that near IRAS 12553 would be filtered out by the data reduction and would not show up in our maps. The different mass recovery fractions could in principle also be due to differences in the dust temperatures. If one assumes that the dust near IRAS 12496 is cooler than the dust near IRAS 12553, then the difference in their mass recovery fractions is smaller than when we assume a common dust temperature. To give an example, a common mass recovery fraction of 50% is inferred when we assume temperatures of 6 K for dust near IRAS 12496 and 16 K for dust near IRAS 12553. Our *Spitzer* images do not allow us to confirm such temperature differences, as the calibration for extended emission is currently uncertain.

The lack of additional detections of compact emission suggests that only a small fraction of the gas in the Cha II complex ($1250 M_{\odot}$ as estimated by Boulanger et al. [1998] from ¹²CO observations) is in compact structures with column densities exceeding 10^{22} cm^{-2} (corresponding to 60 mJy beam^{-1} , the typical

TABLE 3
SEDs OF SELECTED SOURCES IN CHA II

λ (μm)	Flux ^a (mJy)	σ	Reference
IRAS 12496–7650/DK Cha ^b			
70.....	36100	1200	1
1200.....	1470 ^c	120	1
IRAS 12500–7658			
0.643.....	0.0099	0.0009	1
0.805.....	0.061	0.002	1
0.965.....	0.11	0.006	1
1.25.....	0.869	0.06	2
1.6.....	3.56	0.14	2
2.2.....	9.19	0.20	2
3.6.....	20.0	0.19	1
4.5.....	25.6	0.21	1
5.8.....	35.6	0.23	1
8.....	51.0	0.29	1
12.....	110	22	3
24.....	687	4.2	1
25.....	900	180	3
60.....	3630	730	3
70.....	1630	100	1
100.....	5060	1100	3
160 ^d	11800	2400	1
1200 ^c	<260 ^c	...	1
1300.....	59.7	15	4
2MASS 12545753–7649400			
0.643.....	.0896	0.005	1
0.805.....	0.309	0.01	1
0.965.....	1.67	0.15	1
1.25.....	0.407	0.05	2
1.6.....	1.04	0.11	2
2.2.....	1.37	0.12	2
3.6.....	0.92	0.07	1
4.5.....	0.76	0.05	1
5.8.....	1.14	0.07	1
8.....	7.37	0.27	1
24.....	14.5	0.18	1
70.....	302	16	1
2MASS 12560549–7654106			
0.643.....	1.27	0.011	1
0.805.....	3.89	0.033	1
0.965.....	6.34	0.11	1
1.25.....	16.3	0.31	2
1.6.....	27.7	0.51	2
2.2.....	25.4	0.40	2
3.6.....	14.2	0.12	1
4.5.....	9.54	0.09	1
5.8.....	6.50	0.06	1
8.....	3.31	0.04	1
24.....	1.81	0.09	1
IRAS 12553–7651/ISO-Cha II-28			
1.25.....	<0.29	...	2
1.6.....	2.83	0.11	2
2.2.....	36.2	0.70	2
3.6.....	219	3.2	1
4.5.....	342	9.3	1
5.8.....	667	5.8	1
6.7.....	793	26	5
8.....	514	10	1

TABLE 3—Continued

λ (μm)	Flux ^a (mJy)	σ	Reference
IRAS 12553–7651/ISO-Cha II-28			
12.....	700	70	3
14.3.....	1190	25	5
24.....	2500	100	1
25.....	4430	220	3
60.....	10600	530	3
70.....	6720	280	1
100.....	18100	5400	3
160 ^d	27200	2700	1
1200 ^c	1910	130	1
C41			
0.643.....	0.121	0.002	1
0.805.....	0.40	0.007	1
0.965.....	0.69	0.012	1
1.25.....	2.66	0.12	2
1.6.....	<9.64	...	2
2.2.....	<19.0	...	2
3.6.....	22.3	0.32	1
5.8.....	31.7	0.22	1
12.....	90	18	3
24.....	165	1.2	1
25.....	160	32	3
60.....	360	72	3
70.....	123	9.7	1
100.....	3030	610	3
2MASS 13125238–7739182			
0.643.....	2.21	0.019	1
0.805.....	9.08	0.24	1
0.965.....	15.1	0.54	1
1.25.....	40.3	0.85	2
1.6.....	46.6	1.1	2
2.2.....	40.4	0.78	2
24.....	7.89	0.08	1

^a For the IRAC and MIPS 24 and 70 μm data, σ is the flux uncertainty calculated using c2dphot as described in § 3.1.4. The absolute uncertainty in the flux is closer to 10% at 24 μm and 20% at 70 μm . The 160 μm σ reflects a flux uncertainty of 20%. The 1.2 mm σ reflects the statistical noise.

^b IRAS 12496 is saturated at 24 and 160 μm .

^c The 1.2 mm fluxes are aperture fluxes with an 80'' diameter aperture.

^d The 160 μm fluxes are aperture fluxes with a 40'' diameter aperture.

^e The 2 σ upper limit.

REFERENCES.—(1) This work; (2) Cutri et al. 2003; (3) Beichmann et al. 1988; (4) Henning et al. 1993; (5) Persi et al. 2003.

noise level in our maps). This is in line with Mizuno et al. (1999), who speculate that the low column densities in Cha II are responsible for the observed low star formation activity.

5. SELECTED SOURCES IN CHA II

In this section, we highlight a few interesting sources, mainly YSOs, in the Cha II cloud. Most of the sources were originally selected from the MIPS data because they are brighter at 70 μm than 24 μm . The sources 2MASS 12560549–7654106 and 2MASS 13125238–7739182 were selected from Figure 5 as previously unknown YSO candidates as described in § 4.2. C41 was chosen because it was recently noted in the literature by Barrado y Navascués & Jayawardhana (2004).

We present full SEDs, including c2d data from IRAC (A. Porras et al. 2005, in preparation), and some basic physical

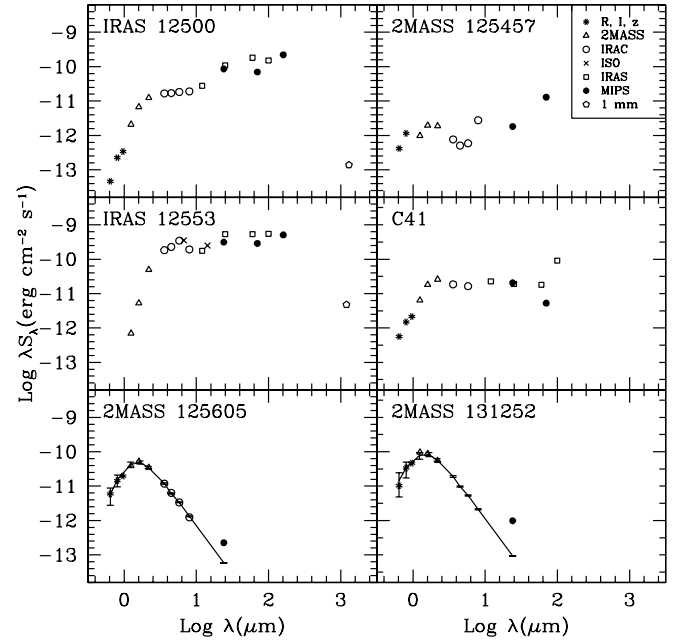


FIG. 12.—SEDs of interesting sources discussed in § 5, including optical data, 2MASS, IRAC, *ISO* (Persi et al. 2003), MIPS, *IRAS* (Prusti et al. 1992; Gauvin & Strom 1992), and 1 mm (IRAS 12500, Henning et al. 1993; IRAS 12553, this work). The key to the symbols is given in the figure. In all cases, the error bars are equal to or smaller than the size of the symbol. The *IRAS* points in the C41 SED are for IRAS 12554–7635, which may or may not be associated with C41. The solid line and error bars in the 2MASS 125605 and 2MASS 131252 panels represent stellar models. The data show excesses over the models at 24 μm , indicating the possible presence of disks.

properties of each source. MIPS positions and fluxes for these sources are listed in Table 2, and the positions are also marked as black squares on Figure 1. SEDs including optical, 2MASS (Cutri et al. 2003), IRAC, *ISO* (Persi et al. 2003), *IRAS* (Beichmann et al. 1988), MIPS, and millimeter-continuum (as described in this work and Henning et al. 1993) data when available are shown in Figure 12, and the fluxes are listed in Table 3. We calculate bolometric luminosities for the sources on the basis of the SEDs shown, assuming that the sources are at the distance of Cha II.

The complementary optical data in the *R*, *I*, and *z* bands were obtained using the wide-field imager at the ESO 2.2 m telescope at La Silla, Chile. The data reduction and photometric calibration were performed as described in Alcalá et al. (2004). The photometric calibration for the *z* band was performed using A0-type standards observed at an air mass very close to 1. The typical seeing was on the order of 0''.9. The source extraction was performed using both DAOPHOT with PSF methods within the IRAF environment and SExtractor (Bertin & Arnouts 1996), with consistent results. More details on these observations will be published in a paper elsewhere (J. M. Alcalá et al. 2005, in preparation).

5.1. IRAS 12500–7658/SSTc2d J125342.8–771512

IRAS 12500–7658 (Prusti et al. 1992) was previously detected by 2MASS (12534285–7715114) and is also visible with IRAC and MIPS. Our SIMBA 1.2 mm map was not sensitive enough to detect IRAS 12500. However, Henning et al. (1993) detected this source at 1.3 mm and classified it as an embedded object. Chen et al. (1997) found that this source has a bolometric temperature, T_{bol} , of 94 K, classifying it as a Class I object according to the scheme of Chen et al. (1995), where Class I objects have $70 \text{ K} < T_{\text{bol}} < 650 \text{ K}$. This source is an outlier on the 2MASS–MIPS color plots (Figs. 5 and 6), because it has a very red

$K_s - [24]$ color of 9.6 mag. The only source with a similarly large $K_s - [24]$ color is a Class I object (IRAS 12553; see § 5.3). IRAS 12500 also has a redder $[24] - [70]$ color (3.3 mag) than most of the 24 μm bright sources, so it is closer to Class I objects (IRAS 12553 and IRAS 13036) in the $[24]$ versus $[24] - [70]$ color-magnitude diagram (Fig. 7) than the bluer Class II objects. Further, IRAS 12500 has a positive $\alpha_{24/K}$ (0.79), also indicating that it is a Class I object. Therefore, the MIPS data are consistent with previous classifications of IRAS 12500 as a Class I protostar. For IRAS 12500 we calculate a bolometric luminosity, L_{bol} , of $0.5 L_{\odot}$ from the SED in Figure 12.

5.2. 2MASS 12545753–7649400/SSTc2d J125457.5–764940

2MASS 12545753–7649400 does not have an *IRAS* source associated with it but was detected in all IRAC bands, as well as MIPS bands 1 and 2. It has a rising SED, as illustrated in Figure 12. However, 2MASS 125457 has a K_s magnitude of 14.2, placing it within the galaxy parameter space on the K_s versus $K_s - [24]$ plot (Fig. 5). This source also has a $[24]$ magnitude of 6.8, which is fainter than most YSOs but consistent with galaxies (Fig. 7). Further, it appears slightly elongated in the IRAC images and clearly looks like a galaxy in the *I*-band image. We conclude that this source is a galaxy, but include it here to illustrate the difficulty of distinguishing YSOs from galaxies based solely on rising SEDs in the mid-infrared. Other diagnostics with data from different wavelengths are needed, such as the color-magnitude diagrams presented here, to begin to separate galaxies from YSOs in MIPS data.

5.3. IRAS 12553–7651/SSTc2d J125906.6–770740

IRAS 12553 (ISO-Cha II-28) is one of the brightest far-infrared sources in Cha II and was the target of a near-IR and ISOCAM study by Persi et al. (2003). It was also detected by 2MASS (2MASS 12590656–7707401), *IRAS* (IRAS 12553–7651; Gauvin & Strom 1992), and at 1.2 mm with SIMBA (see § 4.5). Chen et al. (1997) reported that this source has $T_{\text{bol}} = 99$ K, classifying it as a Class I object. Persi et al. (2003) also classified this source as a Class I protostar on the basis of its spectral index ($\alpha = 1$), with $L_{\text{bol}} = 1.49 L_{\odot}$. We find $L_{\text{bol}} = 1.8 L_{\odot}$ for IRAS 12553 from the SED in Figure 12. The MIPS data confirm the previous classifications of IRAS 12553. This source, like IRAS 12500, has a redder $[24] - [70]$ color (3.5 mag) than known Class II sources (see Fig. 7). IRAS 12553 also has a very red $K_s - [24]$ color (9.5 mag) in Figure 5. Further, we also find a positive spectral index for this source ($\alpha_{24/K} = 0.76$), classifying it as a Class I source.

5.4. C41/SSTc2d J125909.7–765104

C41 was recently proposed to be a classical T Tauri object, with a spectral type of M5.5, near the substellar boundary by Barrado y Navascués & Jayawardhana (2004). They observed broad $H\alpha$ emission, a variety of forbidden lines, and Li I absorption toward C41, which was originally identified as a low-mass YSO candidate by Vuong et al. (2001). It has been detected by 2MASS (2MASS 12590984–7651037), IRAC, and MIPS. C41 is also possibly associated with IRAS 12554–7635 (plotted with the SED for C41 in Fig. 12), which has a T_{bol} of 81 K (Chen et al. 1997) and was classified by Gauvin & Strom (1992) as a Class I source. However, the IRAS 60 and 100 μm fluxes for IRAS 12554 are significantly larger than the MIPS 70 μm flux of C41 (Fig. 12; Table 3) and may be confused. When we include the *IRAS* fluxes in the SED, $L_{\text{bol}} = 0.10 L_{\odot}$, and without the *IRAS* fluxes C41 has an L_{bol} of $0.08 L_{\odot}$. C41 has a very red $K_s - [24]$ color (7.3 mag),

but its color lies between known Class I and Class II sources in Figure 5. In Figure 7, C41 is in the same region as known Class II sources, because its $[24] - [70]$ color is only 2.1 mag.

5.5. 2MASS 12560549–7654106/SSTc2d J125605.5–765411

The source 2MASS 12560549–7654106 was identified by its K_s magnitude (11 mag) and $K_s - [24]$ color (2.0 mag) in Figure 5 as a potential YSO candidate. It also has $\alpha_{24/K} = -2.1$, which suggests that it is a Class III source. However, the K_s magnitude of 11 is fainter than that of typical T Tauri stars at the distance of Cha ($K_s = 8.5$ – 9.5 mag; Gauvin & Strom 1992). The source 2MASS 125605 could not be found in a search of the literature for known YSOs. It was observed by IRAC, 2MASS, and in the optical, and has an L_{bol} of only $0.05 L_{\odot}$. We compared the SED to a stellar model SED for R to 24 μm . The model is that of a star extinguished by about $A_V = 6$ mag and uses the dust model of Weingartner & Draine (2001) with a visual extinction-to-reddening ratio of $R_V = 5.5$. The SEDs of 2MASS 125605 and the model are plotted in Figure 12. The error bars on the model include uncertainties in the A_V and in the spectral type of the star. The SED of 2MASS 125605 is well matched by the stellar SED between R and 8 μm . However, the 24 μm flux exceeds the stellar model prediction by almost a factor of 4. This possible excess and the star's projected position on the cloud suggest that 2MASS 125605 may be a previously unknown YSO with a disk in Cha II. Further observations are needed to confirm its age and excess.

5.6. 2MASS 13125238–773918/SSTc2d J131252.3–773918

The source 2MASS 13125238–7739182 was also identified from the 2MASS-MIPS color-magnitude plot (Fig. 5) as a potential YSO with $K_s - [24] = 3.1$ mag and $K_s = 10.5$ mag, but it has no previous identification in the literature. This source is also fainter at K_s than typical T Tauri stars ($K_s = 8.5$ – 9.5 mag; Gauvin & Strom 1992). Its spectral index, $\alpha_{24/K} = -1.68$, classifies 2MASS 131252 as a Class II object. This source was outside the c2d IRAC observation area in Cha II, so only optical, 2MASS, and MIPS data are available. From its SED, we calculate a low luminosity for 2MASS 131252 of $L_{\text{bol}} = 0.1 L_{\odot}$. We also compared the SED of this source with that of a model of an extinguished star. The 24 μm flux of 2MASS 131252 is more than a factor of 10 greater than that expected from a star with A_V of about 6 mag. This excess suggests that 2MASS 131252 may be a previously unknown YSO with a disk. As with 2MASS 125605, further observations are needed to confirm this conclusion.

6. SUMMARY

We have presented a map of the Cha II molecular cloud at 24, 70, and 160 μm as observed by the *Spitzer* instrument MIPS (Fig. 2) and described in detail the c2d Legacy team's data processing, including removal of artifacts, mosaicking, source extraction, and band merging. We detected over 1500 sources at 24 μm in an area a little over 1.5 deg^2 .

Band-merging the source list with 2MASS and the resulting color-magnitude diagram (Fig. 5) allowed for identification of some of the sources. Galaxies are found to be defined mostly by faint K_s magnitudes (>13 mag). Forty-four sources were found to have $K_s < 13$ mag and $K_s - [24] > 1$ mag and were identified as potential YSOs. An $H - K_s$ versus $K_s - [24]$ color-color diagram (Fig. 6) was found to be ineffective in identifying YSOs because of confusion with galaxies. In a $[24]$ versus $[24] - [70]$ color-magnitude plot (Fig. 7), the data were compared with

models of YSOs from Whitney et al. (2003) and Young & Evans (2005) and found to be bluer than predicted by the models. Calculating a spectral index following the method of Lada (1987) revealed that the same sources identified as YSO candidates in the K_s versus $K_s - [24]$ diagram have $\alpha_{24/K} > -2.5$, providing more evidence that they are YSOs and confirming their identification in the literature. Of these 44 YSO candidates, four have not been previously identified in the literature as YSOs or candidates. The small number of new YSO candidates found with the improved sensitivity of MIPS over previous surveys suggests that most of the YSOs in Cha II are already known. However, future work combining IRAC and MIPS data may reveal more new low-luminosity YSOs.

A SIMBA dust-continuum emission map of Cha II revealed significant emission toward the regions of IRAS 12496 and IRAS 12553 only. The lack of further detections suggests that only a small fraction of the gas is in compact structures with high column density. The extended emission at $160 \mu\text{m}$ was found to be similar to that in *IRAS* and C^{18}O (Mizuno et al. 1999) maps of Cha II.

The SEDs of several YSOs associated with Cha II are presented, including the Class I sources IRAS 12553 and IRAS 12500 (Fig. 12). The SEDs of two new potential YSOs, 2MASS 125605 and 2MASS 131252, were compared with a stellar model and found to have excesses at $24 \mu\text{m}$, indicating the likely

presence of a disk. Follow-up observations are needed to confirm the classification of these previously unknown sources.

Future work will combine the MIPS and SIMBA data sets with optical, near-, and mid-infrared, including IRAC, observations of Cha II to study star formation in the cloud in greater depth. The combined data sets will also allow for better identification and classification of the protostellar and young stellar populations in Cha II.

We would like to thank M. Vuong for providing her extinction map of Cha II. Support for this work, part of the *Spitzer* Legacy Science Program, was provided by NASA through contracts 1224608, 1230782, and 1230779 issued by the Jet Propulsion Laboratory, California Institute of Technology, under NASA contract 1407. K. E. Y. was supported by NASA under grant NGT5-50401 issued through the Office of Space Science. Astrochemistry in Leiden is supported by an NWO Spinoza grant and a NOVA grant. This publication makes use of data products from the Two Micron All Sky Survey, which is a joint project of the University of Massachusetts and the Infrared Processing and Analysis Center at California Institute of Technology, funded by NASA and the National Science Foundation.

REFERENCES

- Alcalá, J. M., Covino, E., Sterzik, M. F., Schmitt, J. H. M. M., Krautter, J., & Neuhäuser, R. 2000, *A&A*, 355, 629
- Alcalá, J. M., Wachter, S., Covino, E., Sterzik, M. F., Durisen, R. H., Freyberg, M., Hoard, D. W., & Cooksey, K. 2004, *A&A*, 416, 677
- Barrado y Navascués, D., & Jayawardhana, R. 2004, *ApJ*, 615, 840
- Beichmann, C., et al., eds. 1988, *IRAS Point Source Catalog* (NASA RP-1190; Washington: GPO)
- Bertin, E., & Arnouts, S. 1996, *A&AS*, 117, 393
- Boulanger, F., Brofman, L., Dame, T. M., & Thaddeus, P. 1998, *A&A*, 332, 273
- Bourke, T. L., Hyland, A. R., Robinson, G., James, S. D., & Wright, C. M. 1995, *MNRAS*, 276, 1067
- Cambrésy, L. 1999, *A&A*, 345, 965
- Chen, H., Grenfell, T. G., Myers, P. C., & Hughes, J. D. 1997, *ApJ*, 478, 295
- Chen, H., Myers, P. C., Ladd, E. F., & Wood, D. O. S. 1995, *ApJ*, 445, 377
- Cutri, R. M., et al. 2003, Explanatory Supplement to the 2MASS All Sky Data Release (Pasadena: IPAC), <http://www.ipac.caltech.edu/2mass/releases/allsky/doc/explsup.html>
- Evans, N. J., II, et al. 2003, *PASP*, 115, 965
- . 2004, First Delivery of Data from the c2d Legacy Project (Pasadena: SSC), <http://ssc.spitzer.caltech.edu/legacy>
- Gauvin, L. S., & Strom, K. M. 1992, *ApJ*, 385, 217
- Gordon, K. D., et al. 2004, *Proc. SPIE*, 5487, 177
- . 2005, *PASP*, 117, 503
- Henning, Th., Pfau, W., Zinnecker, H., & Prusti, T. 1993, *A&A*, 276, 129
- Hughes, J., & Hartigan, P. 1992, *AJ*, 104, 680
- Knee, L. B. G. 1992, *A&A*, 259, 283
- Lada, C. J. 1987, in *IAU Symp.* 115, *Star Forming Regions*, ed. M. Peimbert & J. Jugaku (Dordrecht: Reidel), 1
- Lehtinen, K., & Higdon, J. L. 2003, *A&A*, 398, 583
- Liseau, R., et al. 1996, *A&A*, 315, L181
- Lonsdale, C. J., et al. 2003, *PASP*, 115, 897
- Makovoz, D. 2004, *Spitzer Mosaicker*, Version 1.6 (Pasadena: SSC), <http://ssc.spitzer.caltech.edu/postbcd>
- Mardones, D., Myers, P. C., Tafalla, M., Wilner, D. J., Bachiller, R., & Garay, G. 1997, *ApJ*, 489, 719
- Marleau, F. R., et al. 2004, *ApJS*, 154, 66
- Masci, F. J., Laher, R., Fang, F., Fowler, J., Lee, W., Stolovy, S., Padgett, D., & Moshir, M. 2005, in *ASP Conf. Ser.*, *Astronomical Data Analysis Software and Systems XIV*, ed. P. L. Shopbell, M. C. Britton, & R. Ebert (San Francisco: ASP), in press (astro-ph/0411316)
- Mizuno, A., Onishi, T., Yonekura, Y., Nagahama, T., Ogawa, H., & Fukui, Y. 1995, *ApJ*, 445, L161
- Mizuno, A., et al. 1999, *PASJ*, 51, 859
- Neufeld, D. A., Melnick, G. J., & Harwit, M. 1998, *ApJ*, 506, L75
- Onishi, T., Mizuno, A., Kawamura, A., Ogawa, H., & Fukui, Y. 1996, *ApJ*, 465, 815
- Ossenkopf, V., & Henning, Th. 1994, *A&A*, 291, 943
- Persi, P., Marenzi, A. R., Gomez, M., & Olofsson, G. 2003, *A&A*, 399, 995
- Press, W. H., Teukolsky, S. A., Vetterling, W. T., & Flannery, B. P. 1997, *Numerical Recipes in C* (Cambridge: Cambridge Univ. Press)
- Prusti, T., Wittet, D. C. B., Assendorp, R., & Wesselius, P. R. 1992, *A&A*, 260, 151
- Rieke, G., et al. 2004, *ApJS*, 154, 25
- Schechter, P. L., Mateo, M., & Saha, A. 1993, *PASP*, 105, 1342
- Schwartz, R. D. 1977, *ApJS*, 35, 161
- Sivia, D. S. 1996, *Data Analysis: A Bayesian Tutorial* (Oxford: Clarendon Press)
- Spitzer* Science Center. 2004a, *Spitzer Space Telescope Multiband Imaging Photometer for Spitzer (MIPS) Data Handbook Version 1.1*. (Pasadena: SSC), <http://ssc.spitzer.caltech.edu/mips>
- Spitzer* Science Center. 2004b, *Spitzer Space Telescope Observers Manual*, Version 5.0. (Pasadena: SSC), <http://ssc.spitzer.caltech.edu/documents>
- Surace, J. A., et al. 2004, *The SWIRE ELAIS N1 Image Atlases and Source Catalogs* (Pasadena: SSC), <http://ssc.spitzer.caltech.edu/legacy>
- Tachihara, K., Mizuno, A., & Fukui, Y. 2000, *ApJ*, 528, 817
- Vuong, M. H., Cambrésy, L., & Epchtein, N. 2001, *A&A*, 379, 208
- Wainscoat, R. J., Cohen, M., Volk, K., Walker, H. J., & Schwartz, D. E. 1992, *ApJS*, 83, 111
- Weingartner, J. C., & Draine, B. T. 2001, *ApJ*, 548, 296
- Whitney, B. A., Wood, K., Bjorkman, J. E., & Cohen, M. 2003, *ApJ*, 598, 1079
- Whittet, D. C. B., Assendorp, R., Prusti, T., Wesselius, P. R., & Roth, M. 1991, *A&A*, 251, 524
- Whittet, D. C. B., Prusti, T., Franco, G. A. P., Gerakines, P. A., Kilkeny, D., Larson, K. A., & Wesselius, P. R. 1997, *A&A*, 327, 1194
- Young, C. H., & Evans, N. J., II. 2005, *ApJ*, 627, 293